1    # Retrieval Algorithm for Aerosol Effective Height from the

2    # Geostationary Environment Monitoring Spectrometer (GEMS)

4    Sang Seo Park[1,*], Jhoon Kim[2], Yeseul Cho[2], Hanlim Lee[3], Junsung Park[3], Dong-Won

5    Lee[4], Won-Jin Lee[4], Deok-Rae Kim[4]

6    *[1] Department of Urban and Environmental Engineering, Ulsan National Institute of Science*

7    *and Technology, Ulsan, Korea*

8    *[2]Department of Atmospheric Sciences, Yonsei University, Seoul, Korea*

9    *[3]Division of Earth and Environmental System Sciences, Pukyong National University, Busan,*

10    *South Korea*

11    *[4]Envionment Satellite Center, National Institute of Environmental Research, Incheon, Korea*

15    *Corresponding author. Sang Seo Park (sangseopark@unist.ac.kr)

18    Submitted to Atmospheric Measurement Techniques

19    2023. 06.

**Abstract**

An algorithm for aerosol effective height (AEH) was developed for operational use with observations from the Geostationary Environment Monitoring Spectrometer (GEMS). The retrieval technique uses the slant column density of the oxygen dimer ($O_2$-$O_2$) at 477 nm, which is converted into AEH after retrieval of aerosol and surface optical properties from GEMS operational algorithms. The retrieved AEHs provide continuous vertical information of severe dust plumes over East Asia with reasonably good validation results and the collection of plume height information for anthropogenic aerosol pollutants over India. Compared to the AEH retrieved from Cloud-Aerosol Lidar with Orthogonal Polarization (CALIOP), the retrieval results show bias of -0.03 km with a standard deviation of 1.4 km for the AEH difference over the GEMS observation domain from January to June, 2021. The AEH difference depends on aerosol optical properties and surface reflectance. Compared to the aerosol layer height obtained from the tropospheric monitoring instrument (TROPOMI), differences of 1.50 ± 1.08 km, 1.59 ± 1.22 km, and 1.71 ± 1.24 km were obtained for pixels with single scattering albedo (SSA) < 0.90, 0.90 < SSA < 0.95, and SSA > 0.95, respectively.

Keywords: aerosol effective height, aerosol optical depth, environmental satellite, GEMS

## 1. Introduction

Since the launch of the Total Ozone Mapping Spectrometer (TOMS) on Nimbus-7, ultraviolet (UV)-visible satellite measurements have been used for environmental monitoring of the distribution and reaction processes of pollutants (e.g., anthropogenic aerosols, tropospheric ozone, $NO_2$, and $SO_2$). Measurements from environmental satellites have been used to estimate gaseous species in the atmosphere, resulting in vertical column integrated amounts. However, these column-integrated amounts and associated surface concentrations have uncertainty due to simultaneous changes in optical path length associated with the vertical distribution of target species and amounts of scattering materials (clouds and aerosols) present. In addition, aerosol vertical information is also important for the application of tropospheric concentration of aerosols. For example, aerosol height information in the free troposphere is particularly important for aviation safety by affecting the visibility. Also, scientific applications including radiative forcing studies, long-range transport modelling and studies of cloud formation processes have been used aerosol vertical information as an input parameter.

Environmental satellite sensors, that measure UV-visible wavelength, have been used the UV aerosol index (UVAI) for aerosol detection (e.g., Buchard *et al.*, 2015; Herman *et al.*, 1997; Torres *et al.*, 1998, 2002; Prospero *et al.*, 2000; de Graaf *et al.*, 2005). Furthermore, scattering radiative index values were investigated for the possibility of the cloud signal detection (Penning de Vries *et al.*, 2009, 2015; Kooreman *et al.*, 2020; Kim *et al.*, 2018). However, these indices only have qualitative characteristics and limitations to identify aerosol amounts.

For the quantitative estimation, measurements of aerosol optical depth (AOD) and

67  radiative cloud fraction have also been retrieved from pixel-based radiance data in UV-

68  visible wavelength range. Recently, various aerosol retrieval algorithms have been

69  developed to be applied in passive satellite sensors. These algorithms focus on

70  improved trace gas retrieval as well as direct monitoring of aerosol properties, such as

71  AOD and single scattering albedo (SSA) (e.g., Ahn *et al.*, 2014; Kim *et al.*, 2020; Torres

72  et al., 2020).

73    Although the algorithms developed for environmental satellite sensors indicate the

74  presence and amounts of scattering materials, the accuracy of these retrieval algorithms

75  for trace gases is affected by the relative vertical distributions between trace gases and

76  scattering materials (e.g., Lorente *et al.*, 2017; Hong *et al.*, 2017). For this reason,

77  estimating cloud vertical parameters is important. For cloud vertical information, cloud

78  height information has been estimated simultaneously with cloud optical depth and

79  radiative cloud fraction data using the rotational Raman scattering (Joiner and Vasilkov,

80  2006; Vasilkov *et al.*, 2008; Joiner and Bhartia, 1995) and absorption intensity of the

81  oxygen dimer ($O_2$-$O_2$) (Accarreta *et al.*, 2004; Vasilkov *et al.*, 2018; Choi *et al.*, 2021)

82  combined with normalized radiance.

83    Similarly, the aerosol vertical distribution can be estimated using the oxygen

84  absorption bands, such as the $O_2$-$O_2$ (Park *et al.*, 2016; Chimot *et al.*, 2017; Choi *et al.*,

85  2019, 2020), $O_2$-A (Dubisson *et al.*, 2009; Geddes and Boesch, 2015; Sanders *et al.*,

86  2015; Xu *et al.*, 2017; Zeng *et al.*, 2020), and $O_2$-B (Chen *et al.*, 2021; Ding *et al.*,

87  2016) bands, as well as combinations of these bands (Sanghavi *et al.*, 2012; Chen *et al.*,

88  2021). In addition, an algorithm for aerosol vertical information has been developed

89  based on hyperspectral UV-visible radiance from satellite observation. Nanda *et al.*

90  (2018) demonstrated the possibility of aerosol height retrieval from the $O_2$-A band

91     developed an algorithm using Tropospheric Monitoring Instrument (TROPOMI)

92     (Sanders and de Haan, 2016; Nanda *et al.*, 2020) and implemented the algorithm

93     operationally.

94     However, the vertical distribution of aerosol is difficult to assess because of its large

95     spatio-temporal variability. Although the Cloud-Aerosol Lidar with Orthogonal

96     Polarization (CALIOP) provided the aerosol vertical distribution with high vertical

97     resolution (Omar et al., 2009), other passive satellite sensors are only able to estimate

98     the representative parameter of aerosol height. Veihelmann et al. (2007) showed that the

99     number of degrees of freedom of signal for aerosol is 2-4 for most satellite observation

100     conditions by the ozone monitoring instrument (OMI). In addition, the number of

101     degrees of freedom is not exceeded to 3 from the shortwave satellite measurements (e.g.,

102     Rao et al., 2019; Choi et al., 2021). It means that the amount of information for aerosol

103     vertical distribution has a limitation for satellite sensors. Because of limitation for

104     describing the aerosol vertical information, aerosol layer height (ALH) (e.g., Nanda et

105     al., 2018) or aerosol effective height (AEH) (Park et al., 2016) were defined to retrieve

106     the aerosol vertical information from the passive satellite sensors.

107     The Geostationary Environment Monitoring Spectrometer (GEMS), which was

108     launched by South Korea in February 2020, provides column density of ozone, aerosol,

109     and their precursors (Kim *et al.*, 2020). The main purpose of GEMS is to monitor air

110     quality, and aerosol properties are targets of such monitoring over East Asia. For this

111     reason, the GEMS aerosol algorithm was developed as multiple operational products.

112     The Aerosol algorithm adopted optimal estimation method (Rogers, 2000) to retrieve

113     AOD, SSA, and ALH. Aerosol properties are obtained for the purposes of monitoring

114     air quality and aerosol effects for the air mass factor (AMF) calculation. In addition to

these aerosol products, AEH is provided to represent the upper layer of the peak. Both ALH and AEH help understand the vertical structure of aerosol layer. For the possibility for development of an AEH retrieval algorithm, Park *et al.* (2016) conducted theoretical sensitivity testing of AEH retrieval using solely the $O_2$-$O_2$ absorption band along with aerosol and surface properties. Overall, the sensitivity of AEH retrieval was strongly affected by SSA, AOD, and aerosol types including optical and size properties. In addition, case studies of AEH during dust transport over East Asia were conducted using radiance data from the Ozone Monitoring Instrument (OMI) and aerosol optical properties from the Moderate Resolution Imaging Spectroradiometer (MODIS).

Based on theoretical considerations and case study results, we introduce an operational retrieval algorithm for AEH. Section 2 introduces the details of satellite sensors for the comparison and colocation method in this study. Section 3 describes the details of the AEH retrieval algorithm for GEMS and provides a list of the detailed input parameters. Section 4 reports retrieval results based on case studies of aerosol transport, and section 5 contains long-term validation results based on CALIOP and TROPOMI data. Finally, in section 6, the summary and main conclusions are presented.

**2. Data**

**2.1 GEMS**

The GEMS instrument on board the Geostationary Korea multipurpose satellite 2B (GK2B) is located at 128.2°E, and scans from 145°E to 75°E with north-south coverage of 5°S-45°N. The GK2B observation schedule shares the GEMS and the Geostationary Ocean Color Imager 2 (GOCI2), and the GEMS scan the 30 minutes duration from every hour from 45 minutes to 15 minutes during daytime. The spatial resolution of

GEMS is 3.5 km (North-South) × 8 km (East-West) for aerosol and gaseous products at 38ºN. The spectral range of 300-500 nm is covered with a spectral resolution (as defined by the full-width and half-maximum of the spectral response function) of 0.6 nm and a spectral sampling of 0.2 nm.

The GEMS Level 2 aerosol operational algorithm (L2AERAOD) retrieves the aerosol index (AI) values for UV and visible wavelengths, as well as AOD and SSA after determining the aerosol types (National Institute of Environmental Research, 2020). The aerosol types are defined as absorbing, non-absorbing, and dust types by using the AI based classification methods exploiting measurements in the UV and visible (e.g., Go et al., 2020). Park *et al.* (2016) noted that the error budget of AEH is significantly affected by uncertainty in AOD and SSA and by the misclassification of aerosol types, which is directly related to the optical property and size information. Overall, uncertainties of 0.2 in AOD, of 20% in particle size, of 10% in SSA, and 0.02 in surface albedo cause AEH errors in the range 739-1276 m (Park et al., 2016). In this study, the L2AERAOD results for AOD at 550 nm and SSA at 443 nm were adopted as input data for aerosol properties, and the AOD and SSA values were spectrally converted to those values at assumed wavelength for the inversion calculation process after considering the spectral dependence of the aerosol optical properties by the aerosol models. In addition, we also used the minimum reflectance under the Lambertian assumption to retrieve AOD and AEH to coincide with the use of surface information on L2AERAOD and AEH retrieval.

**2.2. TROPOMI**

TROPOMI is a nadir-viewing spectrometer, the only payload of the Sentinel-5 Precursor (S5P), measuring radiance in the UV, visible, near-infrared, and the shortwave

163 IR (Veefkind et al., 2012). The S5P is a polar orbit satellite that crosses the equator at

164 13:30 local time at an ascending node. The aerosol layer height product from

165 TROPOMI (AER_LH) provides vertically localized aerosol layers in the free

166 troposphere with cloud free condition by using the level 1b earth radiance

167 measurements from 758 to 770 nm (de Graaf *et al.*, 2022). The definition of ALH from

168 TROPOMI is the optical centroid layer height of the plume above sea level. The

169 spectral fit employs a fast forward model based on a neural network for simulated

170 condition of reflectance around the $O_2$-A band. After cloud masking, an optimal

171 estimation method is used to retrieve the ALH and AOD by the inversion method from

172 observation. Other aerosol parameters, such as SSA, layer thickness, and scattering

173 phase function, are assumed to be fixed values (Nanda et al., 2020). Furthermore, the

174 ALH retrieval has limitation to the aerosol plume with higher than 12 km, because the

175 ALH neural network product currently provides the plume pressure range of 75-1000

176 hPa (Michailidis et al., 2023).

177     The main purpose of the AER_LH product is the retrieval of aerosol layers in the free

178 troposphere (desert dust, biomass burning, and volcanic ash) (Michailidis et al., 2023).

179 The target requirement on the accuracy and precision is 0.5 km or 50 hPa, and the

180 threshold requirement is 1 km or 100 hPa under the elevated aerosol plumes with cloud-

181 free conditions for the layer height and for the associated pressure, respectively (de

182 Graaf et al., 2022, Veefkind et al., 2012). However, the TROPOMI ALH product has

183 strong dependence of the surface albedo, especial to the bright surfaces (Sanders et al.,

184 2015). From Michailidis et al. (2023), a mean bias of -0.51±0.77 and -2.27±1.17 km is

185 estimated over ocean and land, respectively. In this study, we use version 02.04.00 of

186 the TROPOMI offline level 2 AER_LH product (European Space Agency, 2021) with

187   the spatial resolution is 3.5 km × 5.5 km at nadir viewing geometry.

188

**2.3. CALIOP**

190   The CALIOP is a spaceborne lidar onboard the Cloud-Aerosol Lidar and Infrared

191   Pathfinder Satellite Observations (CALIPSO) to measure the vertical information of

192   aerosol and cloud with estimating the optical properties. The CALIOP has two different

193   wavelength channels (532 and 1064 nm) by using the Nd:YAG laser to generate the

194   signals (Winker et al., 2009). The CALIPSO is Sun synchronous orbit constellated to

195   the A-train with period of 98.3 minutes. It crosses the equator at 13:30 local time on an

196   ascending node. To cover the GEMS observation area, we used CALIOP data of 3-4

197   orbits per day. For the vertical information, the resolution for vertical sampling is 30 m

198   below 8 km altitude, and 60 m from 8 to 20 km altitude, respectively. Although the

199   CALIOP retrieves the data with extremely high horizontal and vertical resolutions, the

200   spatial coverage is narrow because the footprint of the CALIOP is about 90 m at the

201   Earth surface. In this study, the data of Level 2 aerosol profile product (APro, version

202   3.41) was used (Tackett et al., 2018). The aerosol profile product simultaneously

203   includes both aerosol and cloud optical depth. In addition, extinction quality flag

204   (Extinction_QC_Flag) data shows the quality of extinction profile. In this study, we

205   checked and used the quality flag value at 532 nm for the aerosol extinction coefficient

206   profile data. The AOD from CALIOP is vertically integrated aerosol extinction

207   coefficient from surface to top of atmosphere, and representative layer height

208   parameters (ALH and AEH) are directly estimated by using the vertical profile of

209   aerosol extinction coefficient at 532 nm to minimize the spectral discrepancy of aerosol

210   extinction. For the ALH retrieval, we adopted mean extinction height from the CALIOP

211 extinction coefficient profile (e.g., Koffi et al., 2012; Xu et al., 2019). Similarly, the

212 AEH estimation from CALIOP is also used to the extinction coefficient profile.

213

214 **2.4 Data Selection and Colocation**

215     In this study, we used data within 75°E-145°E for east-west and 5°S-45°N for north-

216 south direction, which is the observation area of GEMS. From Park et al. (2020), the

217 spatial range of highly coincident AOD is 30-40 km. To ensure that the number of

218 retrieved observation pixels that can be analyzed in this study is sufficiently high, we

219 relax the spatial limits for colocation matching. For spatial colocation, we selected

220 pixels for which distance between GEMS and CALIOP (or TROPOMI) observations

221 was less than 50 km. In addition, only the closest 10% of pixels were used. Given the

222 different orbital characteristics of CALIOP (or TROPOMI) and GEMS, temporal

223 colocation was also considered. During the period of image scanning from east to west

224 over Asia by GEMS, CALIOP and TROPOMI pass through the GEMS observation area

225 from south to north every 98.3 minutes. On average, two low earth orbit (LEO)

226 satellites pass three to four orbits through the GEMS scan area during a single day of

227 daytime observation. To consider these different orbital characteristics, only

228 observations taken within ±1 hour of the GEMS observation time was selected for

229 temporal colocation. As GEMS observes hourly, colocated pixels between the two

230 satellites shift from east to west over time.

231     To ensure the accuracy of ALH from TROPOMI, only pixels with quality assurance

232 (QA) values of 1.0 were used. To minimize the cloud contamination, the TROPOMI

233 ALH product uses the VIIRS cloud mask information and cloud parameters from the

234 Fast Retrieval Scheme for Clouds from the Oxygen A-band (FRESCO). To consider the

235     cloud contamination for the aerosol products, in addition, the VIIRS cirrus cloud

236     reflectance (viirs_cirrus_reflectance < 0.4), VIIRS cloud mask (viirs_cloud_mask < 0.1),

237     and cloud fraction from the FRESCO (cloud_fraction < 0.1) are considered in this study

238     (Michailidis et al., 2023). However, de Graaf *et al.* (2022) showed that respective cloud

239     masking methods have difficulty detecting various clouds. For this reason, cloud

240     contamination remains a critical source of uncertainty in the ALH retrieval. From

241     previous studies, the UVAI is used to detect the presence of absorbing aerosol (e.g.,

242     Chen et al., 2021; Griffin et al., 2020; Michailidis et al., 2023; Sanders et al., 2015), and

243     the aerosol height information was only retrieved on the absorbing aerosol pixels.

244     However, the GEMS aerosol product is retrieved not only the absorbing aerosols, but

245     also the non-absorbing aerosols. For this reason, the pixels for which with an AOD at

246     443 nm ($AOD_{443}$ hereafter) taken from the GEMS aerosol product exceed 0.3 are

247     selected for AEH retrieval.

248

249     **3. AEH retrieval algorithm**

250     AEH is a layer height parameter that considers the penetration of photons into the

251     aerosol layer. It is defined such that the integral of the vertical aerosol extinction profile

252     from the surface to the AEH is equal to $(1-e^{-1}) \times$ AOD, as defined by Park *et al.* (2016).

253     Numerous previous studies have used the aerosol top layer height (Kohkanovsky and

254     Rozanov, 2010) or middle layer height (i.e. ALH or centroid height) (e.g., Sanders *et al.*,

255     2015; Nanda *et al.*, 2020) as the aerosol vertical layer parameter. AEH is similar to the

256     aerosol top layer height but with a slight bias.

257     For AEH retrieval, the vertical distribution assumption is also important. The

258     Gaussian Density Fitting (GDF) distribution, which is a modified Gaussian distribution

259 structure by considering the range of upper and lower boundary height, is assumed for

260 AEH retrieval. The full-width at half-maximum (FWHM) of the aerosol layer is

261 assumed to be 1 km. A schematic description of AEH and other aerosol vertical

262 parameters are shown in Figure 1. Based on the assumptions about the aerosol vertical

263 distribution, the AEH value is higher than the peak height of the Gaussian distribution

264 and lower than the aerosol top layer height. Otherwise, the ALH is defined as the

265 integral of the vertical aerosol extinction profile from the surface to the ALH is equal to

266 0.5 × AOD. This assumption is used by Nanda et al. (2016). Therefore, the ALH equals

267 the peak height of the profile in the conditions shown in Figure 1.

268
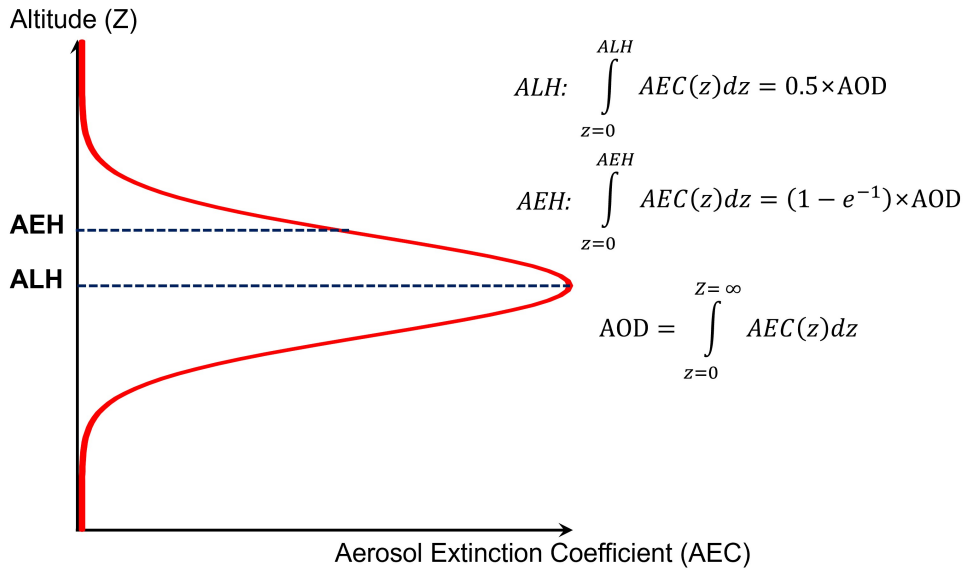
269 **Figure 1.** A schematic illustration of AEH and ALH definitions in an idealized

270 Gaussian shape of aerosol vertical distribution.

271
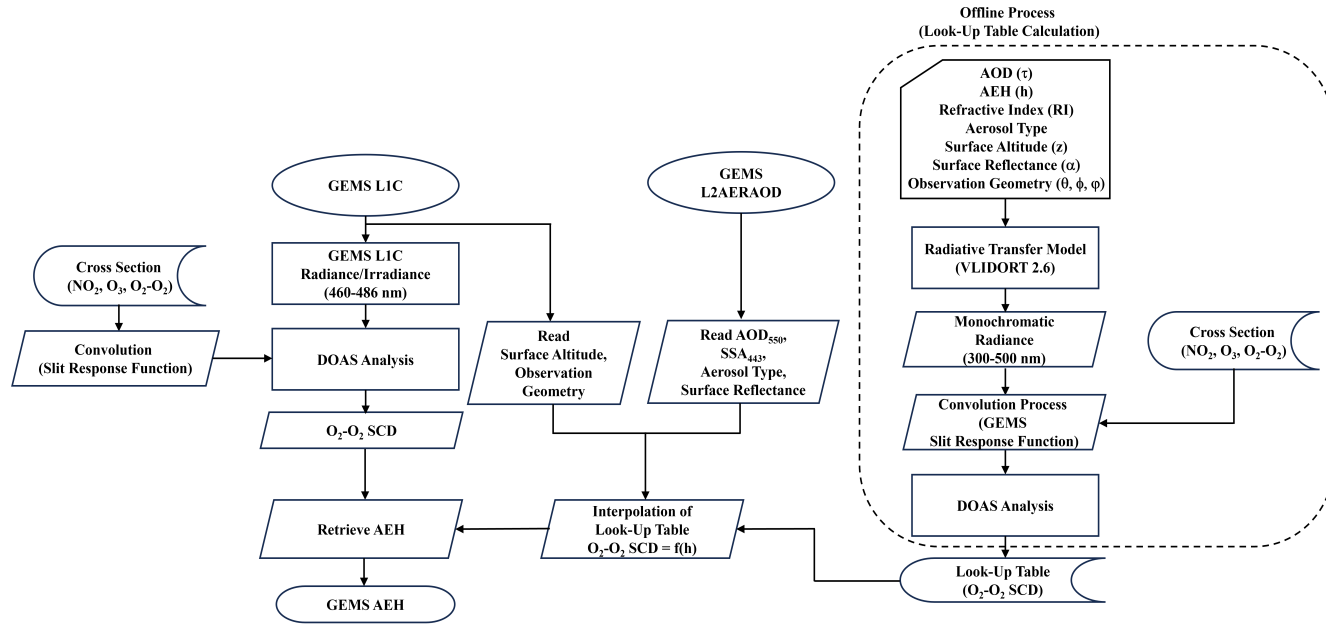
272    **Figure 2.** Flowchart of the AEH retrieval algorithm for GEMS satellite observation.

273

274    For AEH retrieval, the basic idea is the identification of changes in optical path length

275    caused by effective aerosol layer height variation. To measure the optical path length

276    change, $O_2$-$O_2$ SCD retrieved by the DOAS method was used because the spectral

277    coverage is limited to 300-500 nm (Park et al., 2016, Kim et al., 2020). In the GEMS

278    product, the $O_2$-$O_2$ SCD at 477 nm absorption band is the most useful absorption band

279    because this absorption band is strongest absorption band within the GEMS spectral

280    observation range. Figure 2 shows the overall flowchart of the AEH algorithm for

281    GEMS satellite. The AEH algorithm for GEMS employs a look-up table (LUT) that

282    contains $O_2$-$O_2$ slant column density (SCD) values for many scenarios with a variety of

283    observation geometries [solar zenith angle (SZA; $\theta$), viewing zenith angle (VZA; $\Phi$),

284    relative azimuth angle (RAA; $\varphi$)], surface altitude (z), surface reflectance ($\alpha$), AOD ($\tau$),

285    AEH (h), Refractive Index (RI) for SSA, and aerosol type. During the radiance

286    simulation, the radiance is monochromatically simulated and then convolved with the

287    GEMS instrument spectral response function. Finally, the radiance information is

288    converted to the $O_2$-$O_2$ SCD from differential optical absorption spectroscopy (DOAS)

289    method (Platt, 1994).

290    DOAS method has been frequently used to estimate the amount of trace gases (i.e.,

291    SCD of trace gas) from ground (e.g., Cheng et al., 2023; Irie et al., 2008; Platt and Stutz,

292    2008; Wagner et al., 2011; Wang et al., 2017) and satellite (e.g., Kwon et al., 2019; Li et

293    al., 2023; Wagner et al., 2007, 2010) measurements. Detailed DOAS fitting parameter

294    and setting information is provided in Table 1 for the estimation of $O_2$-$O_2$ SCD from

295    both the simulation and observation data. For the $O_2$-$O_2$ SCD estimation at 477 nm, the

296    fitting window ranges from 460 to 486 nm to cover the full absorption structure of $O_2$-

297    $O_2$. Within the fitting window, the absorptions of $NO_2$ and $O_3$ are significant. To

298    describe these two absorbing species, temperature dependent cross section information

299    is adopted. The temperature dependent cross section setting considers stratosphere and

300    troposphere, simultaneously.

301

302    **Table 1.** Details of fitting parameter for $O_2$-$O_2$ SCD estimation via the DOAS method.

| Parameter | |
|---|---|
| **Fitting window** | 460 – 486 nm |
| **Absorption cross section** | $NO_2$ at 220 and 294 K (Vandaele *et al.*, 1998) |
| | $O_3$ at 223, 243 and 293K (Bogumil *et al.*, 2001) |
| | $O_2$-$O_2$ at 293 K (Thalman and Volkamer, 2013) |
| | Ring |

303

304

**Table 2.** Ratio between SCD error and the SCD of $O_2$-$O_2$ according to the polynomial order and offset settings used for DOAS fitting.

| Polynomial | Offset = none | Offset = $0^{th}$ |
|---|---|---|
| $2^{nd}$ order | $6.06 \pm 2.07$ | $6.79 \pm 2.31$ |
| $3^{rd}$ order | $6.32 \pm 2.20$ | $6.79 \pm 2.32$ |
| $4^{th}$ order | $7.86 \pm 2.78$ | $7.34 \pm 2.85$ |

To minimize the noise effect and improve DOAS fitting quality, the optimal settings for fitting were also analyzed. Table 2 shows ratios of $O_2$-$O_2$ SCD error to the $O_2$-$O_2$ SCD for various polynomial and bias orders from observed radiance. The polynomial and offset are basic fitting parameters for the DOAS fitting. Two parameters describe the broadband spectral feature of radiance before identifying the gas absorption structure. The ratio between SCD error and the SCD of $O_2$-$O_2$ is important to determine the AEH retrieval quality. When the fitting error increases, the uncertainty of AEH is also enhanced during the retrieval. Smallest AEH fitting errors are obtained by a DOAS fit with a $2^{nd}$ order of polynomial, and 'none' offset. These settings are used in the GEMS AEH algorithm.

In estimating AEH, other aerosol characteristics, including AOD and aerosol optical properties, affect retrieval accuracy. Park et al. (2016) have shown that the largest contributor to the AEH uncertainty is associated with the uncertainty in SSA. In addition, the AEH retrieval uncertainty due to error in the aerosol optical properties (e.g., AOD and phase function) and surface reflectance has dependence on observation geometries. After the estimation of $O_2$-$O_2$ SCD, for this reason, conversion from $O_2$-$O_2$

324    SCD to AEH is an essential process. Table 3 shows dimensions of the LUT for the AEH

325    retrieval algorithm. To calculate the LUT, a linearized pseudo-spherical vector discrete

326    ordinate radiative transfer model (VLIDORT) version 2.6 was used (Spurr, 2013).

327    During the radiative transfer model simulation, reference wavelength for the SSA and

328    AOD is assumed to be 440 nm. The aerosol type is defined by the radiative absorptivity

329    and particle size information. The aerosol type is classified as absorbing, dust, and non-

330    absorbing aerosol. Absorbing and non-absorbing aerosol types are assumed to be the

331    fine-mode dominant particles. For the spectral conversion of AOD, the angstrom

332    exponents of 1.186, 0.222, and 1.179 are used for absorbing, dust, and non-absorbing

333    aerosol, respectively. The SSA is assumed to be spectrally constant within the spectral

334    range for $O_2$-$O_2$ estimation. Although the spectral $O_2$-$O_2$ absorption band is around 477

335    nm, the spectral discrepancy between reference wavelength for aerosol optical

336    properties and center wavelength of $O_2$-$O_2$ absorption is assumed to be ignored in this

337    study. After calculating spectral radiance with 0.1 nm sampling, the convolution with

338    the GEMS slit response function was applied, and the spectra were sampled on the

339    spectral grid of the GEMS radiance data (Level 1C) prior to the DOAS fitting. Radiative

340    transfer calculations were performed accounting for the temperature dependence of

341    absorption cross section for $O_2$-$O_2$ (e.g., Park *et al.*, 2017).

342

343

344

345

346

347

348    **Table 3.** The dimension of the LUT for the GEMS AEH retrieval algorithm used to

349    estimate AEH from $O_2$-$O_2$ SCD. (SZA: solar zenith angle, VZA: viewing zenith angle,

350    RAA: relative azimuth angle, SUR: surface reflectance).

| Variable [unit] | No. of entries | Entries | |
|---|---|---|---|
| **Spectral range [nm]** | - | 455-491 nm (0.1 nm interval) | |
| **SZA [º]** | 7 | 0.01, 10, 20, 30, 40, 50, 60 | |
| **VZA [o]** | 7 | 0.01, 10, 20, 30, 40, 50, 60 | |
| **RAA [o]** | 10 | 0.01,20, 40, 60, 80, 100, 120, 140, 160, 180 | |
| **SUR** | 3 | 0.0, 0.05, 0.2 | |
| **AOD at 440 nm** | 11 | 0.04, 0.2, 0.4, 0.7, 1.0, 1.3, 1.6, 2.0, 2.5, 3.0, 5.0 | |
| **Refractive Index (Imaginary) at 440 nm** | 3×3 | **Absorbing** (Real: 1.45) | 0.000, 0.0074, 0.0314 |
| | | **Dust** (Real: 1.53) | 0.0, 0.0030, 0.0080 |
| | | **Non-Absorbing** (Real: 1.41) | 0.0, 0.0040, 0.0156 |
| **AEH [km]** | 13 | 0.0 (Extrapolate), 0.2, 0.5, 1.0, 1.3,1.6, 2.0, 2.3, 2.7, 3.0, 3.5, 5.0, 10.0 (Extrapolate) | |
| **Terrain Height [km]** | 2 | 0.0, 2.0 | |

351
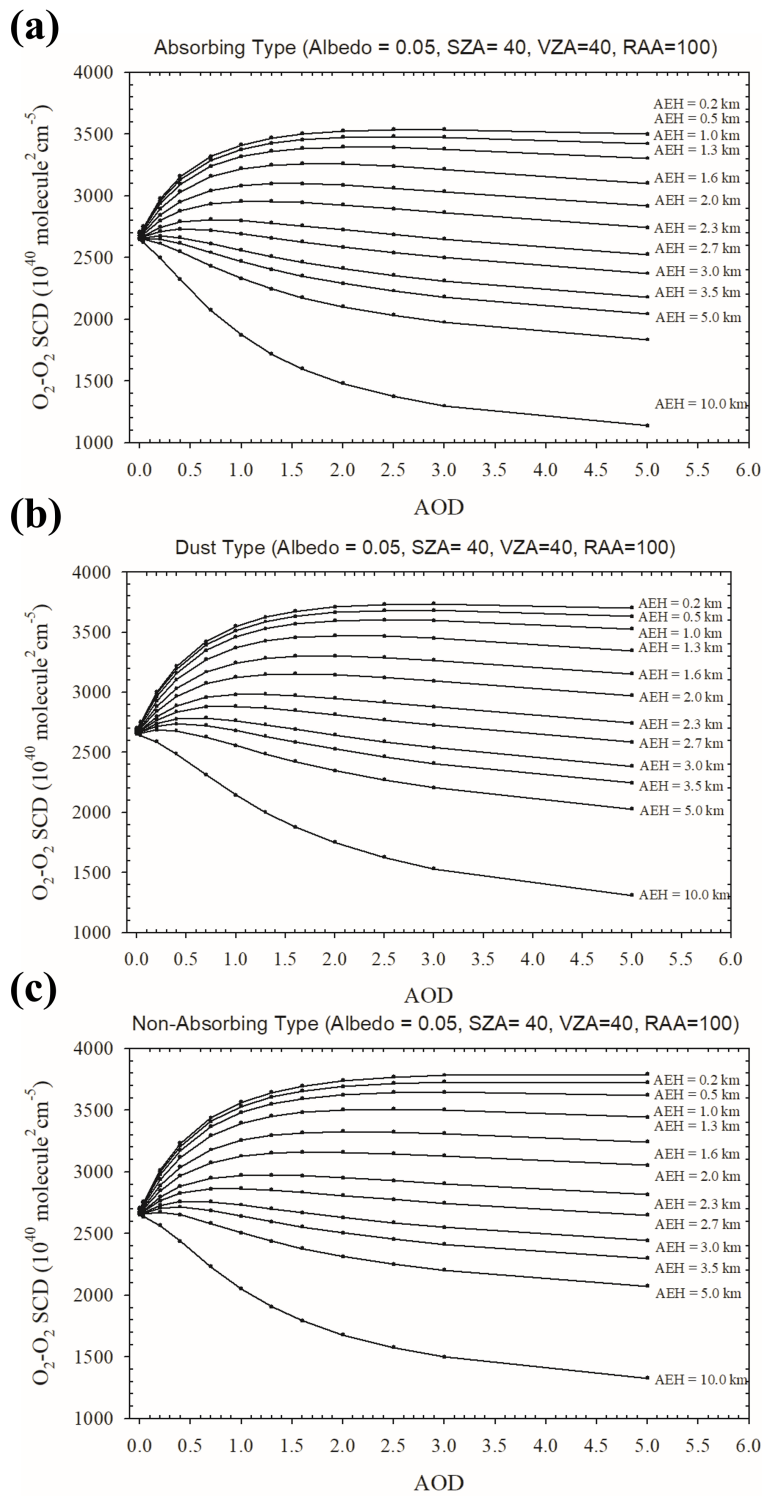
**Figure 3.** O$_2$-O$_2$ SCD dependence as a function of AOD and AEH for (a) Absorbing,

(b) Dust, and (c) Non-Absorbing aerosol types.

354

355    Figure 3 shows the example of $O_2$-$O_2$ SCD dependence as a function of AOD and

356    AEH from the LUT according to the respective aerosol types and AOD. $O_2$-$O_2$ SCD

357    decreases with increasing AEH for all aerosol types and AOD (Park *et al.*, 2016).

358    Similar to the previous study, the $O_2$-$O_2$ SCD sensitivity is enhanced at high AOD and

359    absorbing aerosol cases from GEMS LUT. In addition, the contrast of $O_2$-$O_2$ SCD is

360    greater for absorbing aerosols than non-absorbing aerosols. During the radiance passing

361    through the aerosol layer, the absorbing aerosol is more efficiently absorbed the

362    radiance. For this reason, the effective optical path length is significantly shorter for

363    absorbing aerosols.

364    The AEH algorithm used the GEMS operational AOD and surface reflectance.

365    However, those retrieval results include the uncertainties. Figure 4 shows the AEH

366    retrieval uncertainty based on the $O_2$-$O_2$ SCD LUT with an AOD error of 0.2. The

367    retrieval uncertainty of AEH was evaluated as the relative ratio of SCD changes with

368    respect to input variables. This ratio is defined by the relationship between changes in

369    SCD per unit AEH and changes in SCD due to uncertainties in input variables. The

370    AOD error of 0.2 is twice the target accuracy of the GEMS standard algorithm product.

371    Because the $O_2$-$O_2$ SCD change is small in high AOD, the AEH retrieval uncertainty is

372    relatively small in high AOD condition. In addition, the SCD sensitivity in high AEH is

373    weak due to the vertical distribution characteristics of $O_2$-$O_2$. Thus, the AEH uncertainty

374    is up to 0.9 km at high AEH case in moderate AOD cases (around 0.5-1.0).

375    Figure 5 shows the AEH retrieval uncertainty with the surface reflectance error of

376    0.02. Because surface reflection and aerosol scattering simultaneously affect the

377    increase in optical path length, surface reflectance uncertainty has a significant impact

378    especially to low AOD. The AEH retrieval error due to uncertainty in surface

379    reflectance is larger than 1 km in cases with AOD < 0.4. In addition, the AEH error by

380    the surface reflectance uncertainty linearly decreases with increasing AOD, indicating

381    relatively small impact with aerosol height change.
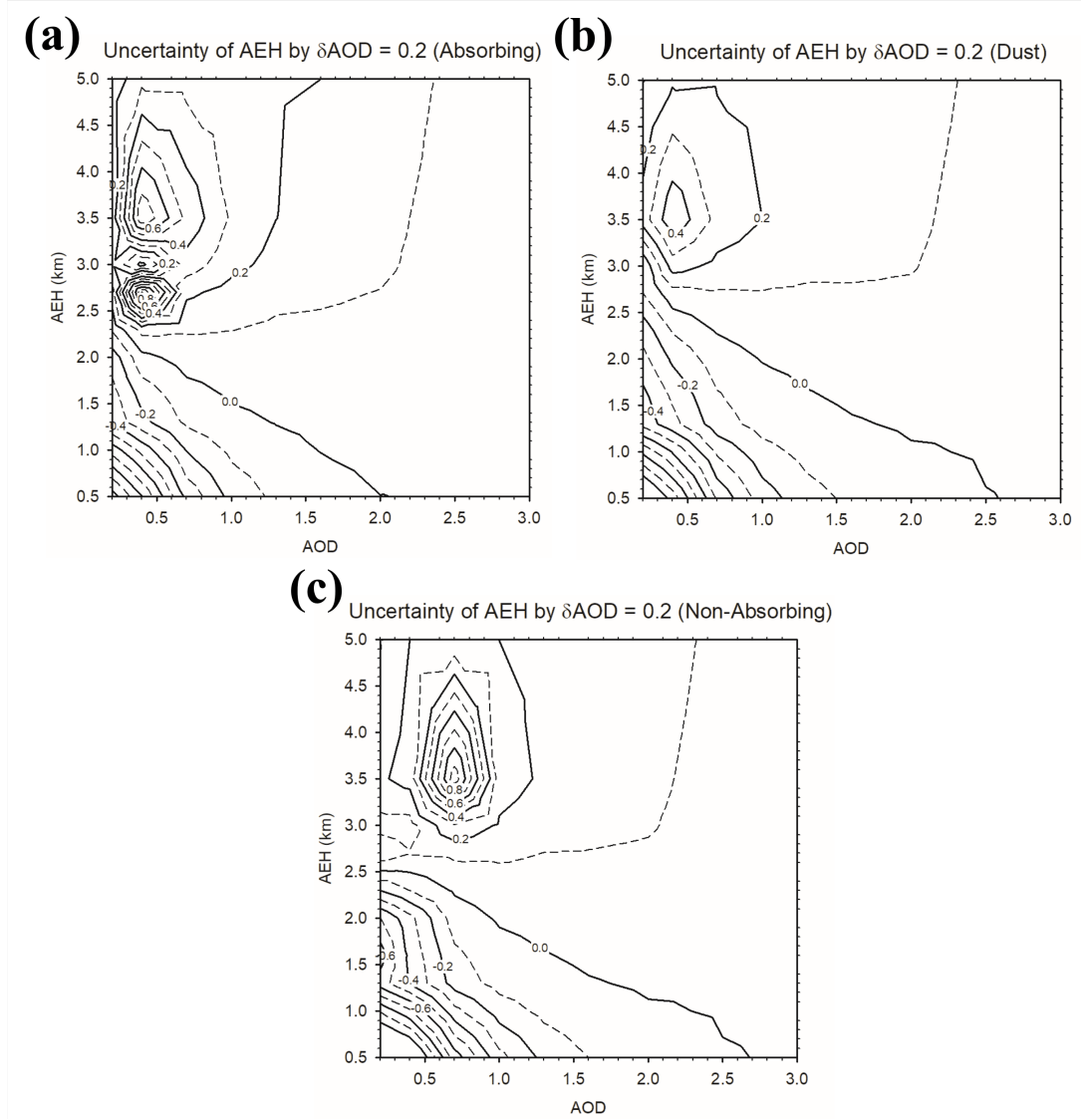
382

383    **Figure 4.** AEH retrieval uncertainty due to the AOD error of 0.2 for cases with (a)

384    Absorbing, (b) Dust, and (c) Non-Absorbing aerosol types.

385
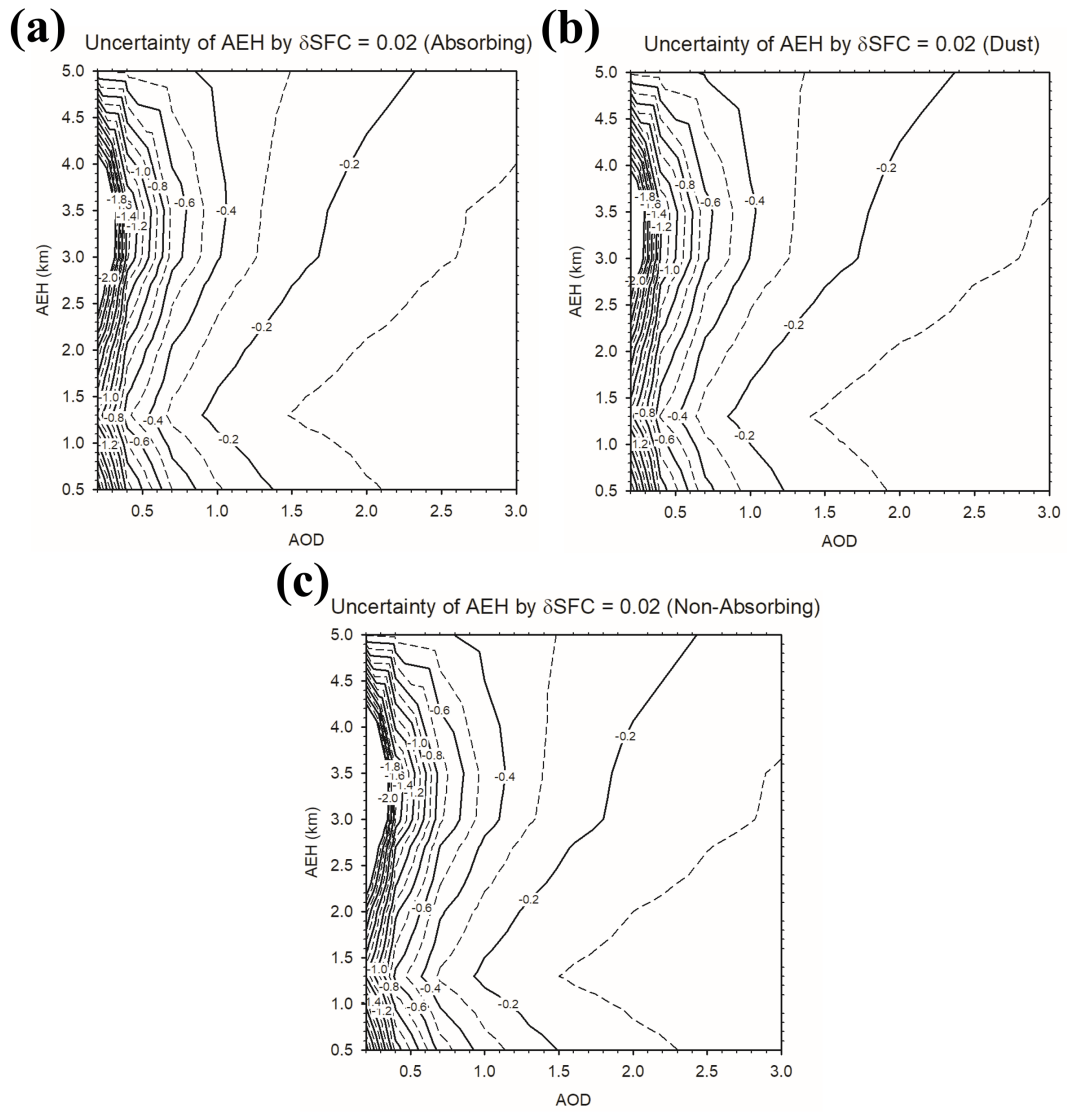
**Figure 5.** AEH retrieval uncertainty due to the surface reflectance error of 0.02 for

386

cases with (a) Absorbing, (b) Dust, and (c) Non-Absorbing aerosol types.

387

388

389
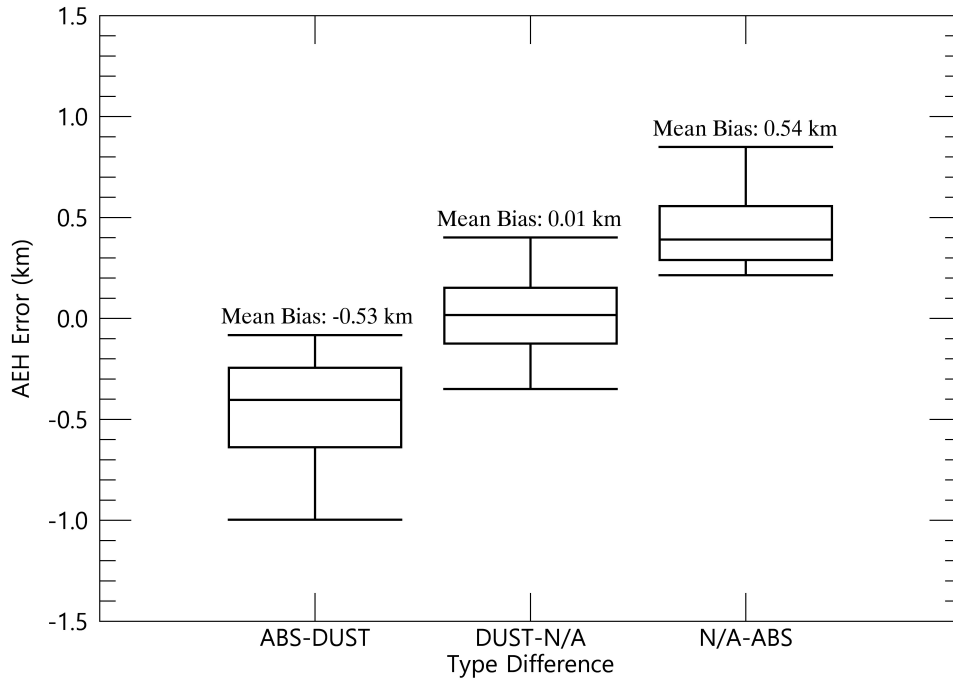
**Figure 6.** AEH retrieval uncertainty caused by the aerosol type misclassification.

391

Figure 6 shows the retrieval uncertainty caused by misclassification of the aerosol types. On average, the AEH retrieval uncertainty takes values up to 0.5 km, but this uncertainty shows larger than 2 km under low AOD and short optical path length conditions. From the sensitivity analysis, aerosol type (in terms of SSA) and AOD, and surface reflectance are carefully considered as input parameters for AEH retrieval.

In the AEH retrieval, the AOD, aerosol type, and SSA are obtained from the L2AERAOD, which is standard aerosol product of GEMS. The aerosol vertical distribution is always fixed as GDF function profiles as shown in Spurr and Christi (2014).

401

402

403    **4. Case studies**

404    Figure 7 shows retrieval results for AEH from GEMS on March 29 over East Asia.

405    Because the operational schedule is hourly during the daytime, the GEMS retrieval

406    results are shown at 1-hour intervals from 01:00 to 07:00 Universal Time Coordinated

407    (UTC). $AOD_{443}$ and SSA at 443 nm ($SSA_{443}$ hereafter) are also shown in Figures S1 and

408    S2, respectively. Pixels with low $AOD_{443}$ values have large AEH uncertainty due to

409    weak aerosol scattering information (see also Park *et al.*, 2016). For this reason, only

410    AEH retrieval results with AOD greater than 0.3 are shown in this study. In addition, the

411    AEH retrieval results are only shown to the "Reliable" quality flag of L2AERAOD,

412    which is estimated to the aerosol optical properties with significant averaging kernel for

413    optimal estimation in L2AERAOD. A case was analyzed in which a dust plume was

414    located along the coast of China and South Korea with $AOD_{443}$ of 0.8-1.2.

415    Simultaneously, another plume was also present over the northeastern Korean Peninsula

416    with $AOD_{443}$ of 1.0-2.0. $SSA_{443}$ was 0.90-0.93 for the plume over South Korea and

417    0.87-0.90 for the plume over the northeastern Korean Peninsula. Retrieved AEH results

418    from these different plumes show similar ranges. For both detected plumes, the AEH

419    shows similar patterns and takes values ranging between 1.0 and 2.0 km in this case.

420
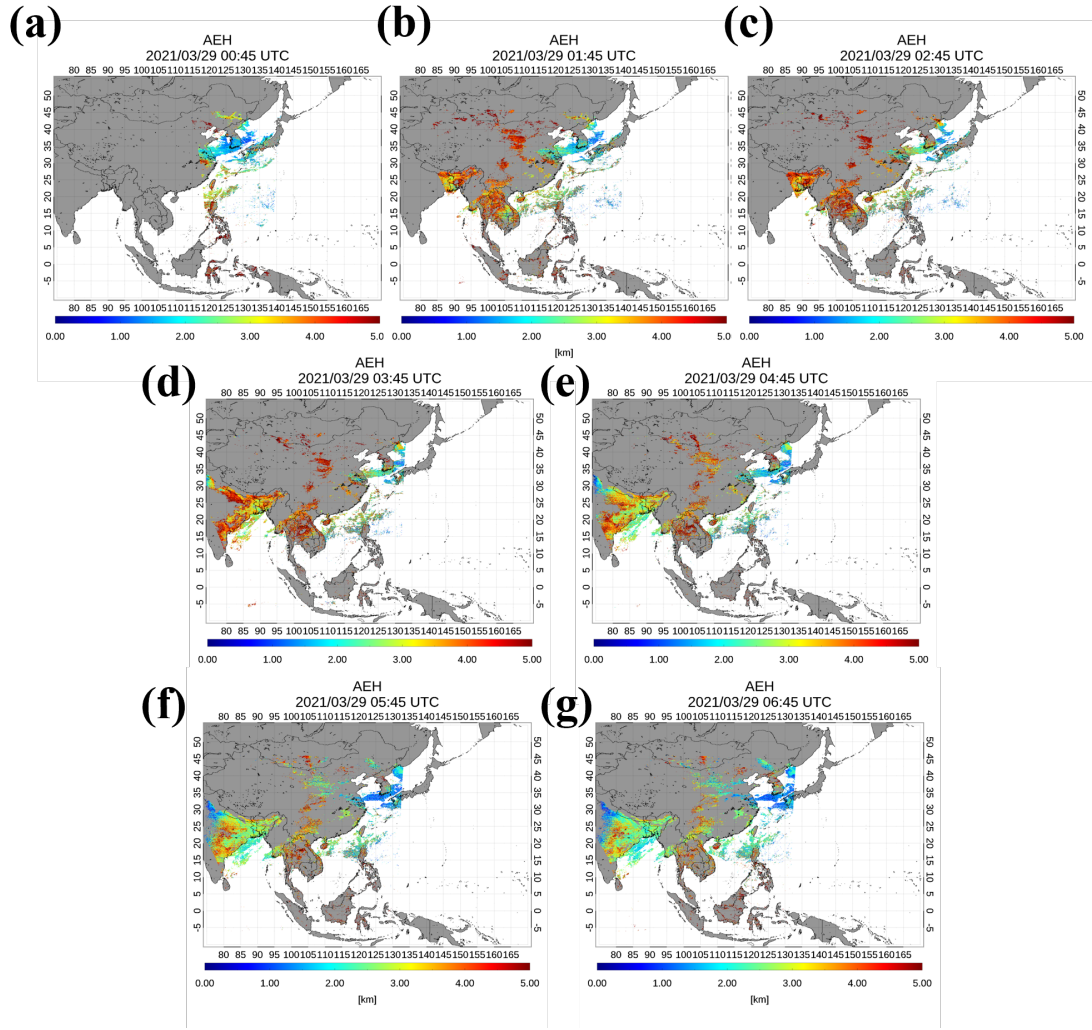
**Figure 7.** Case study results for AEH based on GEMS observations on March 29, 2021 [(a) 00:45 UTC, (b) 01:45 UTC, (c) 02:45 UTC, (d) 03:45 UTC, (e) 04:45 UTC, (f) 05:45 UTC, and (g) 06:45 UTC].

An additional severe aerosol plume was present over northeastern India, with $AOD_{443}$ of 1.0-2.0 and $SSA_{443}$ of 0.85-0.90. According to Rana *et al.* (2019), metropolitan cities and industrial clusters in India are heavy emitters of black carbon, and high concentrations of black carbon are distributed over the Indo-Gangetic Plain (IGP). Therefore, the aerosol plume with high AOD and low SSA (high absorbing) is

430  considered a physical rather than an artifact due to edge of GEMS observation field.

431  Except for the inland parts of India, AEH in high AOD pixels ranged from 1.5 to 3.5 km.

**(a)** TROPOMI ALH 2021/03/28   **(b)** TROPOMI ALH 2021/03/29
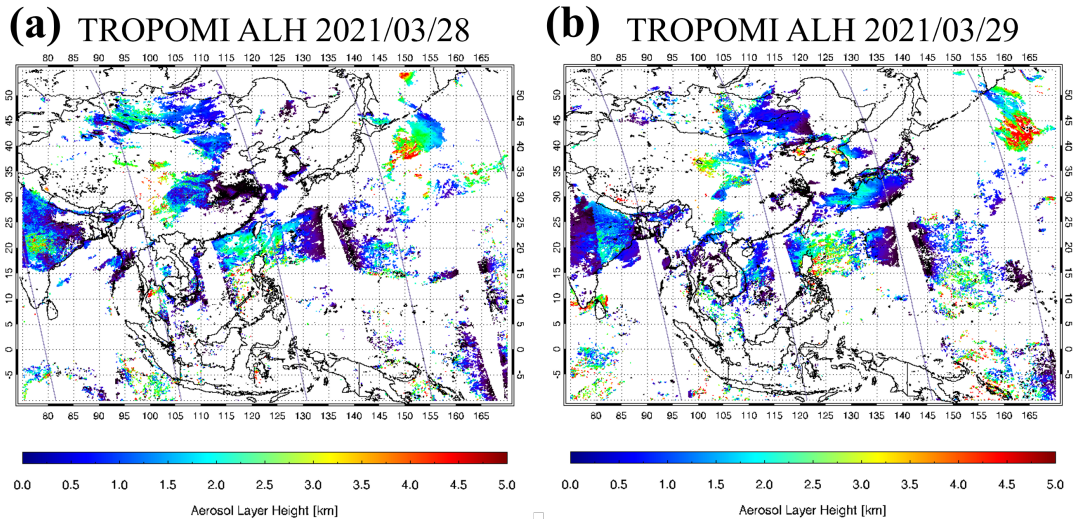
433  **Figure 8.** ALH retrieved from TROPOMI and orbit path of CALIOP on (a) March 28

434  and (b) March 29, 2021 (Unit: km).

435

436  For comparison of the retrieval, Figure 8 shows the ALH retrieved from TROPOMI

437  on March 28 and 29, 2021 over East Asia. A dust plume was transported from China to

438  South Korea during this period, then split into two distinct plumes over northeastern

439  China and the coastal area of South Korea. The ALH retrieved from TROPOMI for both

440  plumes range between 0.5 and 1.5 km. Given the difference in definition for the aerosol

441  height parameters between ALH and AEH as shown in Fig. 1, AEH values retrieved

442  from GEMS were higher than the ALH values retrieved from TROPOMI. In an ideal

443  case under symmetric gaussian distribution with a width of 1 km, the AEH from GEMS

444  was around 0.5 km higher than the peak height of aerosol layer. The ALH expresses the

445  center (or peak) height, thus, the AEH from GEMS was overestimated by around 0.5 km

446  relative to the ALH from TROPOMI. Although AEH had higher values than ALH from

447    TROPOMI, the GEMS AEH retrieval provided meaningful physical results for the dust

448    transport case study.

449
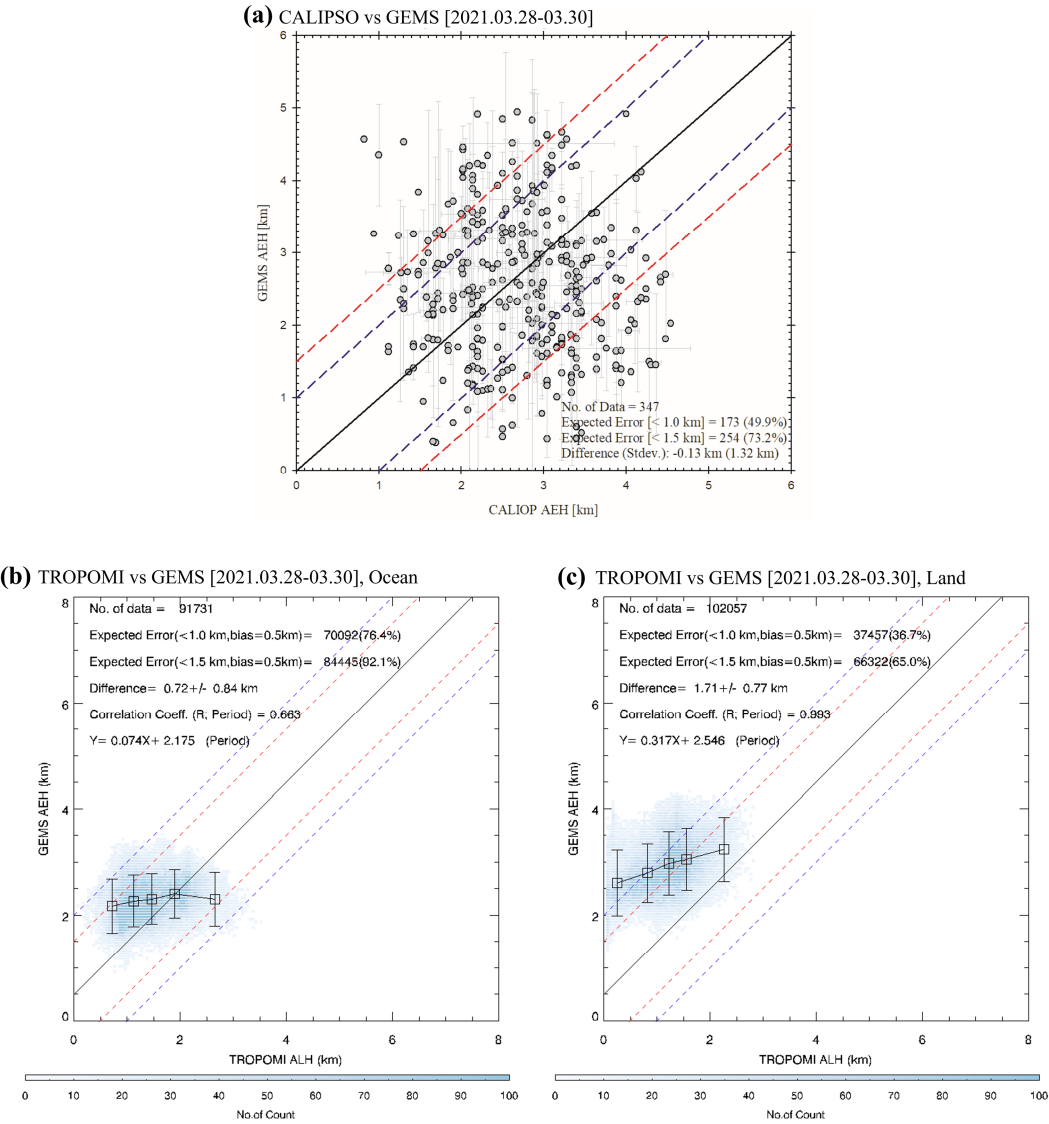
450    **Figure 9.** Intercomparison of (a) AEH between CALIOP and GEMS and (b) ALH

451    from TROPOMI and AEH from GEMS over ocean and (c) over land (Black box and

452    error bar is mean and standard deviation in 20% interval of each TROPOMI ALH) over

453    the period from March 28 to 30, 2021.

454

455    Figure 9 shows intercomparison results for aerosol plume height among GEMS,

CALIOP, and TROPOMI during the case study of dust transport in East Asia from March 28 to 30, 2021. For the direct comparison shown in Figure 9a, the difference in AEH between GEMS and CALIOP was -0.13±1.32 km. Nanda *et al.* (2020) reported that the difference in ALH between TROPOMI and CALIOP was 0.53 km for 4 cases of thick Saharan dust plumes. Large AEH uncertainty occurred mostly over the inland area of China. Because AEH from GEMS uses only the $O_2$-$O_2$ absorption band, the accuracy of AEH is sensitive to uncertainty in surface reflectance and AOD. From Park et al. (2016), total error budget of AEH is 0.74-1.28 km, and the total error budget considered the uncertainty of AOD, SSA, aerosol particle size, and surface reflectance in the aerosol retrieval process. The total error budget amount from the previous study is similar value of standard deviation of AEH difference between GEMS and CALIOP.

Figures 9b and 9c illustrate the comparison results between GEMS AEH and TROPOMI ALH, for the period of March 28-30, 2021, over land and ocean surface, respectively. The difference between GEMS AEH and TROPOMI ALH was 0.72 ± 0.84 km and 1.71 ± 0.77 km over ocean and land in this case, respectively. In addition, 82.4% and 37.3% of all pixels had differences of less than 1.5 km over ocean and land, respectively. However, the ALH from TROPOMI is generally lower than the AEH from GEMS because of the discrepancy in definitions. Based on the assumption of aerosol vertical distribution for AEH retrieval, the difference between AEH and center height of aerosol extinction profile is around 0.5 km. To consider the inconsistency of definition between ALH and AEH, the difference between two retrieval results decreased to 0.5 km bias. After consideration of definition inconsistency, the proportion of pixels within the expected error ranges of 1.5 km are enhanced to 92.1% and 65.0% over ocean and land, respectively.

480
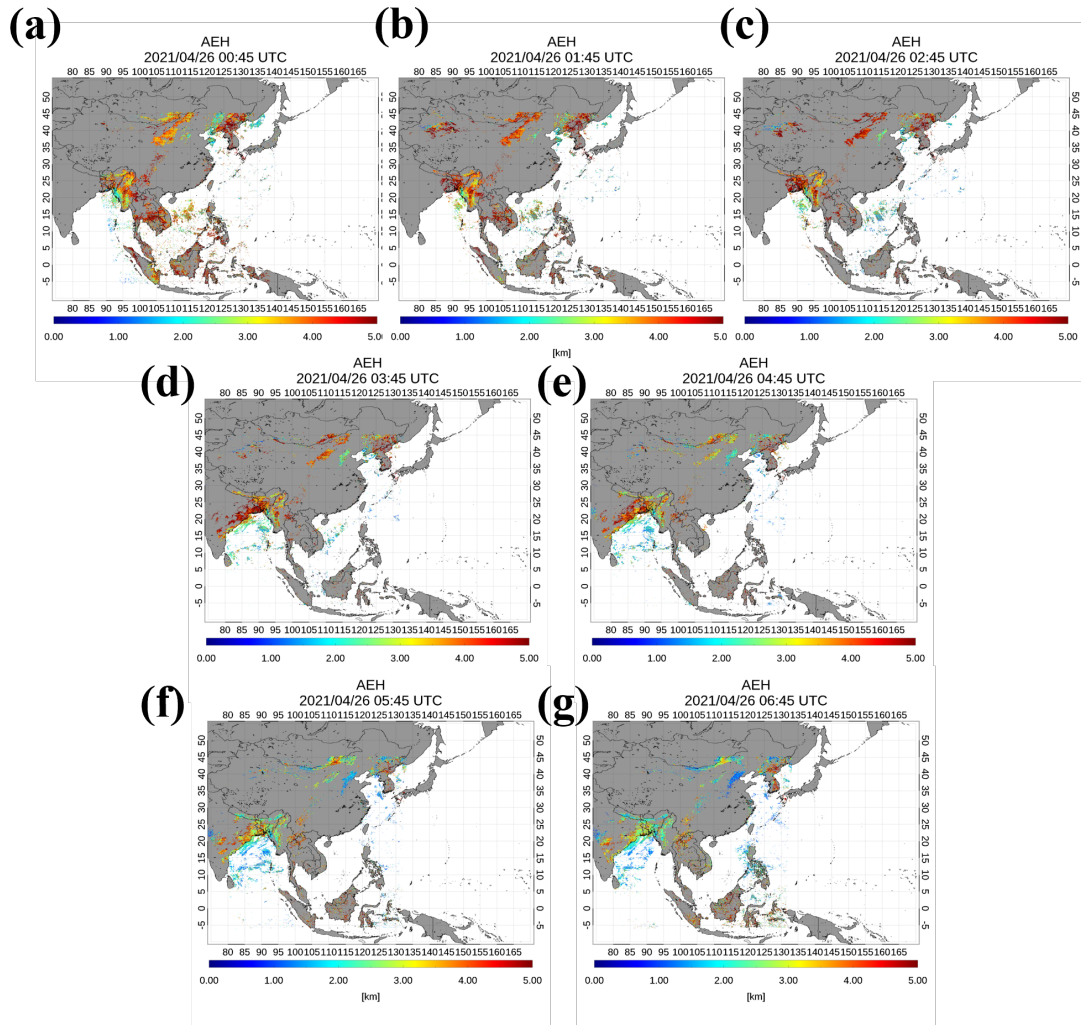
**Figure 10.** Case study results for AEH based on GEMS observations on April 26, 2021 [(a) 00:45 UTC, (b) 01:45 UTC, (c) 02:45 UTC, (d) 03:45 UTC, (e) 04:45 UTC, (f) 05:45 UTC, and (g) 06:45 UTC].

TROPOMI ALH 2021/04/26

484
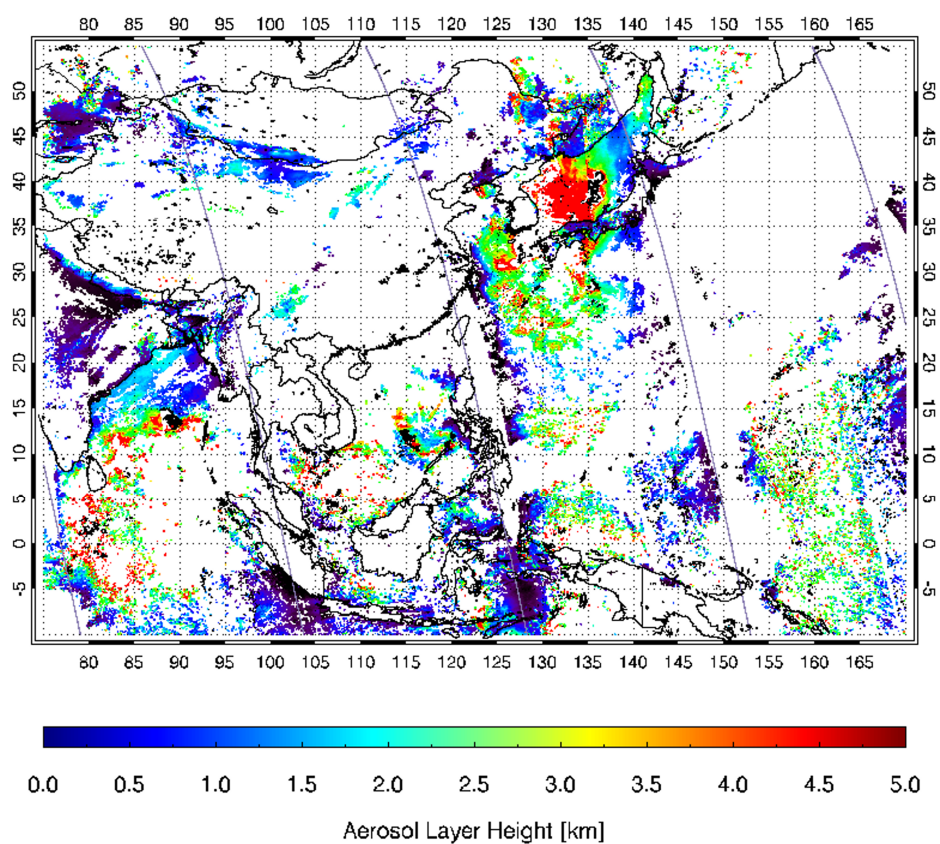
485     **Figure 11.** ALH retrieved from TROPOMI and orbit path of CALIOP on April 26,

486     2021 (Unit: km).
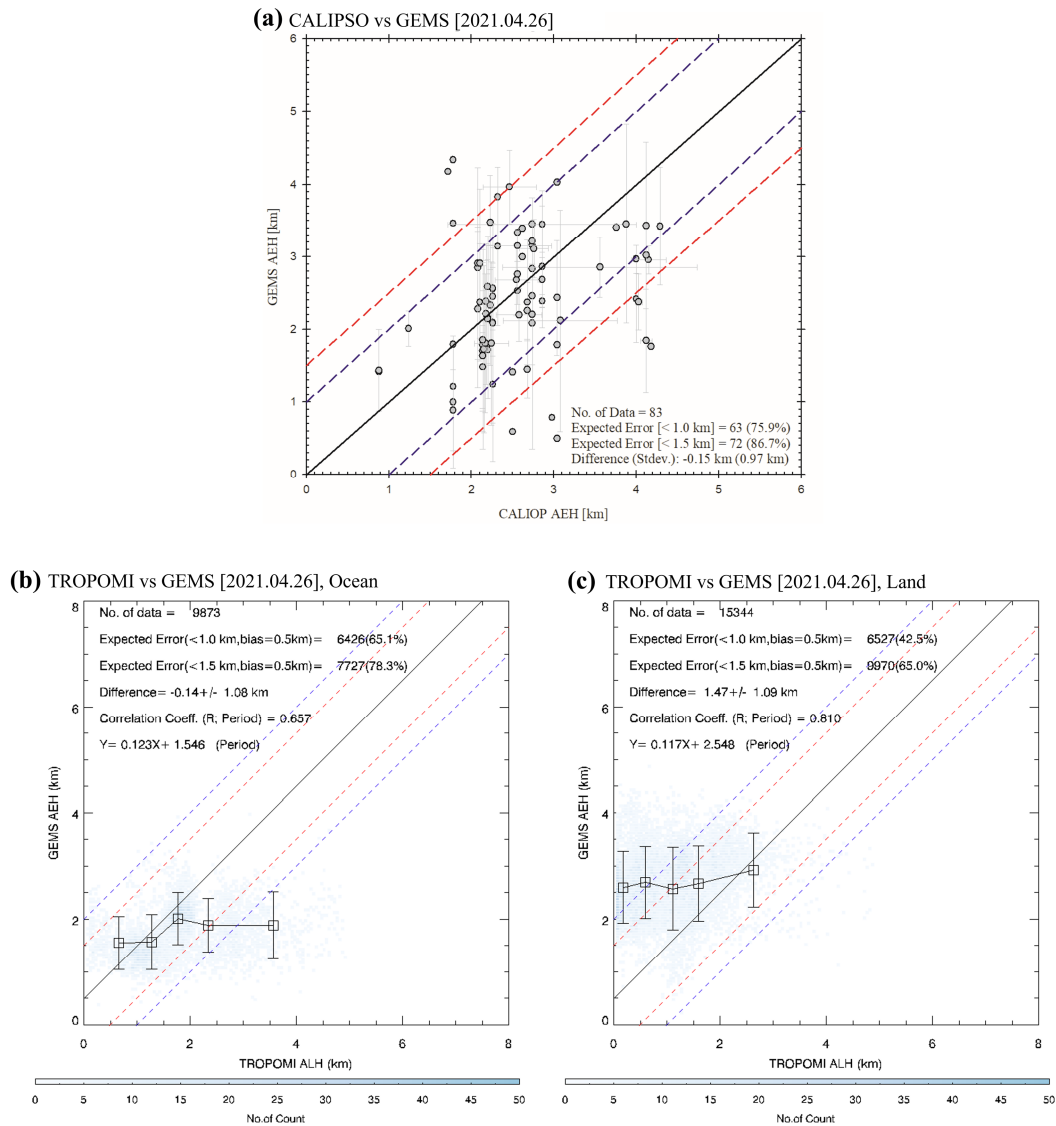
**Figure 12.** Intercomparison of (a) AEH between CALIOP and GEMS, and (b) ALH from TROPOMI and AEH from GEMS over ocean and (c) over land (black dot and error bar is mean and standard deviation in 20% interval of each TROPOMI ALH) on April 26, 2021.

An additional intercomparison case of April 26, 2021, is shown in Figures 10 (GEMS) and 11 (TROPOMI). During the transport of the dust plume from inland China to the coastal area, AEH changed from 4.0 km at 02:00 UTC to 2.0 km at 06:00 UTC.

496   By contrast, ALH from TROPOMI only observed the 1.5-2.5 km layer height over East

497   Asia around 04:00 UTC. Although the AEH from GEMS had spatio-temporal

498   uncertainty, this case demonstrates the advantage of AEH retrieval from GEMS for

499   continuous monitoring of changes in plume height during dust transport, in particular.

500   As shown in Figure 12, AEH from GEMS showed differences in height of -0.15 ± 0.97

501   km (compared to CALIOP). In addition, the differences in height of -0.14 ± 1.06 and

502   1.47 ± 1.09 km over ocean and land as compared to TROPOMI ALH.

503   From two different case results, proportion values within 1.0 km (or 1.5 km) height

504   difference between TROPOMI and GEMS have strong dependence of surface types.

505   The proportion over land (over ocean) was lower (higher) than the corresponding result

506   from the comparison of GEMS and CALIOP. The TROPOMI ALH from version 2

507   exhibits a strong surface type dependence as compared to the ground lidar data

508   (Michailidis et al., 2023). However, the relationship between TROPOMI ALH and

509   GEMS AEH in 20% interval of each TROPOMI ALH have high correlation coefficients.

510   In the case of March 28-30, the correlation coefficients between TROPOMI and GEMS

511   are 0.663 and 0.993 over ocean and land, respectively. In the case of April 26, the

512   correlation coefficients are 0.657 and 0.810 over ocean and land, respectively.

513

514   **5. Long-term validation**

515   For long-term validation, we used the AEH retrieval results from January to June,

516   2021. The CALIOP and TROPOMI satellites passed over the study area around 13:30

517   local time, which is around 04:30 UTC for East Asia and around 06:30 UTC for India.

518   Most temporal colocation pixels aligned with observation times of 04:00-06:00 UTC,

519   respectively. To check the dependence of several retrieval variables, the UVAI, AOD,

520  SSA, and dominant aerosol type in each pixel (TYPE) were obtained from the

521  L2AERAOD. Although the GEMS algorithm retrieved AEH in the range of 0-10 km,

522  the sensitivity of $O_2$-$O_2$ SCD to the optical path length was weak in cases of high AEH

523  because the vertical distribution of $O_2$-$O_2$ SCD is related to the square of the air

524  molecule densities. To ensure sufficient quality of retrieved data, therefore, the AEHs

525  from GEMS and CALIOP, and the ALH from TROPOMI were used only in pixels

526  where the AEH from GEMS were lower than 5 km.

527
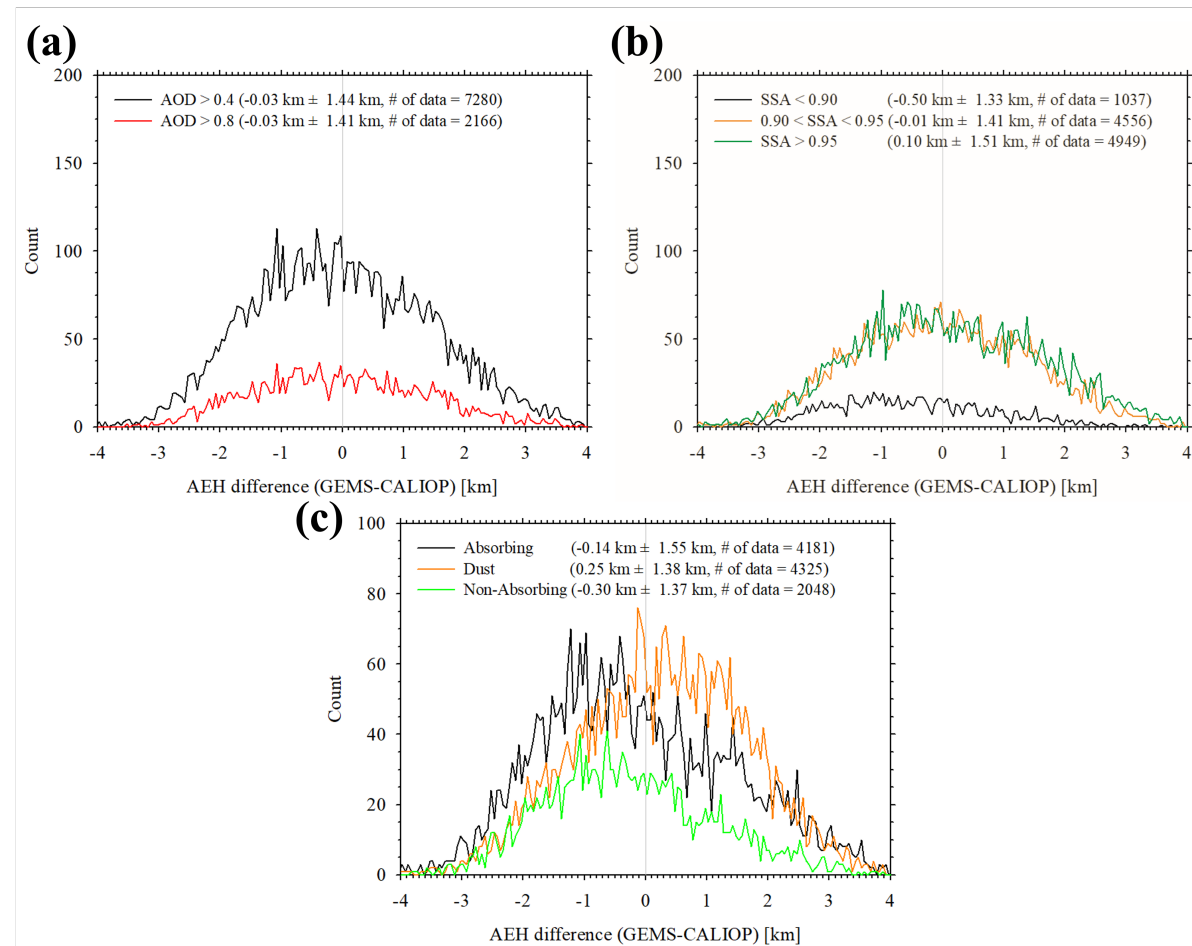
528  **Figure 13.** Histogram of AEH difference between CALIOP and GEMS with respect

529  to (a) AOD, (b) SSA, and (c) TYPE from GEMS over the period from January 1 to June

530  30, 2021.

531    Figure 13 shows histograms of difference in AEH between GEMS and CALIOP

532    according to $AOD_{443}$, $SSA_{443}$, and TYPE from GEMS. From Figure 13a, the

533    dependence on AOD threshold was insignificant; the average estimated AEH difference

534    was -0.03 km, but the variation in AEH difference was around 1.4 km based on the

535    standard deviation for $AOD_{443} > 0.4$. Because of uncertainty in GEMS aerosol

536    operational products, AEH from GEMS exhibits large variability. Although

537    L2AERAOD from GEMS retrieved the AOD, SSA, and aerosol types, the retrieved

538    results from L2AERAOD include significant uncertainty. Go et al. (2020) reported that

539    the root-mean square error (RMSE) of AOD between MODIS and OMI UV aerosol

540    algorithm is 0.276-0.341.

541    In addition, fitting error perturbs the fitting signals and tends to result in the

542    underestimation of SCD. Although the fitting error of $O_2$-$O_2$ SCD from GEMS radiance

543    was minimized, the fitting error has still remained around 6%, as indicated in Table 2.

544    The discrepancy in fitting condition between the simulated and observed radiance

545    biased the SCD estimation, which in turn led to bias and variation in the AEH retrieval.

546    Combined with the high sensitivity of AEH errors to aerosol optical properties,

547    uncertainty arising from L2AERAOD causes AEH variability.

548    The variation in AEH difference between observation platforms is shown in Figure

549    13b as a histogram according to SSA threshold. Across the entire SSA threshold range,

550    the standard deviation of the AEH difference was 1.33-1.51 km. In particular, this

551    standard deviation decreased slightly with decreasing SSA. The aerosol height

552    parameter is more sensitive to absorbing-dominant aerosols than scattering-dominant

553    aerosols (e.g., Park *et al.*, 2016; Nanda *et al.*, 2020). For this reason, the variability of

554    AEH is smaller in absorbing-dominant aerosols than scattering-dominant aerosols, if the

555    uncertainty of other aerosol parameters (AOD, SSA, and TYPE) is the same conditions.

556    Figure 13c shows the dependence of AEH difference on TYPE. The TYPE product

557    included dependence on the aerosol size and optical absorptivity. For this reason, the

558    AEH difference graphs for the "Dust" and "Absorbing" types differ, despite both types

559    being absorbing-dominant aerosols. The AEH difference for the "Absorbing" type

560    showed a negative bias with a large standard deviation, whereas a positive bias with a

561    small standard deviation was obtained for the "Dust" type. The AEH difference for the

562    "Non-Absorbing" aerosol type showed the largest negative bias in this comparison.

563    These results suggest that the aerosol size distribution of fine particles affects the

564    negative bias of AEH. Combined with the AEH difference bias illustrated in Figure 8b,

565    these findings indicate that the bias in AEH difference for "Absorbing" aerosols is

566    weakened by their absorbing-dominant property.

567    Figure 14 shows means and standard deviations for AEH difference between

568    CALIOP and GEMS according to AOD and AI values from GEMS. For AOD, the mean

569    AEH difference ranged from -0.13 to 0.03 km with a standard deviation of

570    approximately 1.45 km. Similar to Figure 13a, the variation in AEH difference with

571    AOD change was insignificant. For the AI, the lowest AEH difference was -0.19 km,

572    obtained for the AI range of 1.5-2.0. The largest AEH difference was 0.24 km for the AI

573    range of 4.0-4.5. Although the AEH difference varied slightly, no consistent tendency in

574    AEH variation with AI was observed. Overall, the standard deviation of AEH difference

575    ranged from 1.49 km (0.0 < AI < 0.5) to 1.18 km (4.5 < AI < 5.0), and a consistent

576    tendency of decreasing variance in AEH difference was found with increasing AI.

577
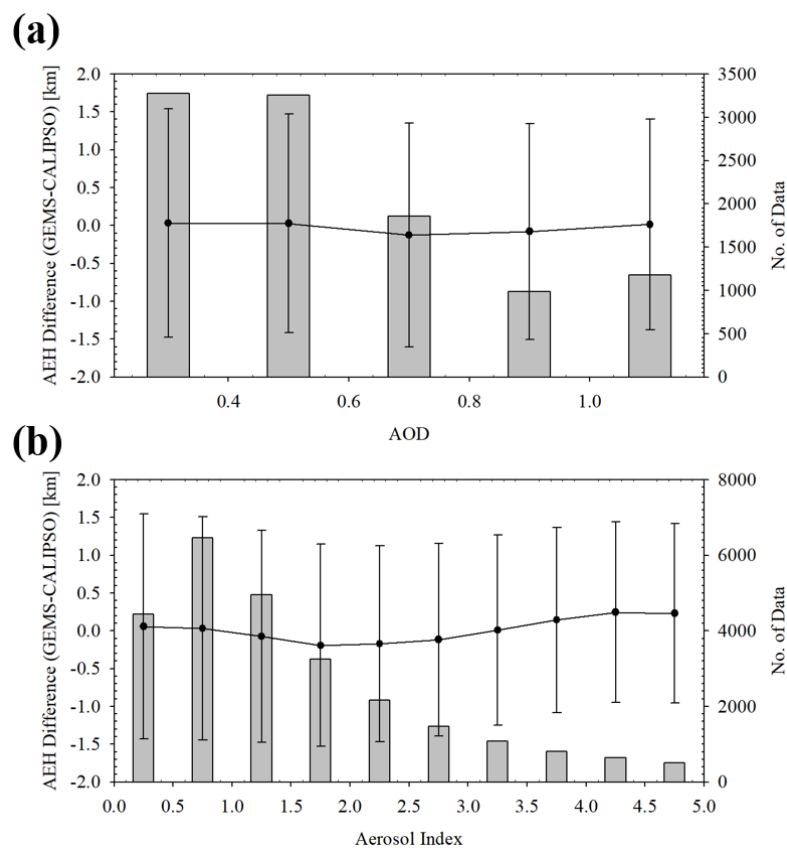
**Figure 14.** AEH difference between CALIOP and GEMS with respect to ranges of (a) AOD and (b) AI obtained from GEMS from January 1 to June 30, 2021 (Black dots and error bars denote the mean and standard deviation of AEH difference, while the gray-box indicates the number of data).

582

583
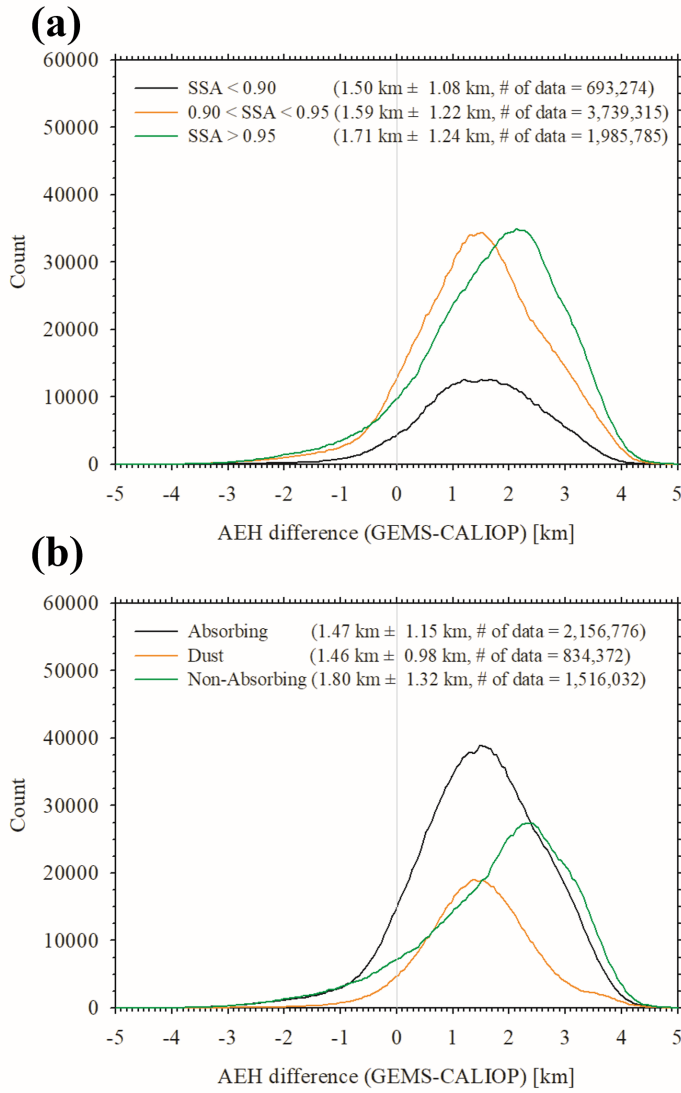
**Figure 15.** Histograms of differences between TROPOMI ALH and GEMS AEH with respect to (a) SSA, and (b) TYPE from GEMS in the period from January 1 to June 30, 2021.

587

Figure 15 shows histograms of differences between GEMS AEH and TROPOMI ALH according to the $SSA_{443}$ and TYPE obtained from GEMS. The difference between GEMS AEH and TROPOMI ALH depends on both SSA and TYPE. The mean difference value between GEMS AEH and TROPOMI ALH decreased as the aerosol

592    absorptivity increased. This difference was $1.50 \pm 1.08$, $1.59 \pm 1.22$, and $1.71 \pm 1.24$ km

593    for pixels of $SSA_{443} < 0.90$, $0.90 < SSA_{443} < 0.95$, and $SSA_{443} > 0.95$, respectively.

594    Comparing these results to Figure 13b, we find that the standard deviation of the

595    comparison with TROPOMI was approximately 75% of the corresponding value for

596    CALIOP. It is because both TROPOMI and GEMS are passive sensors that use similar

597    retrieval methods for oxygen absorption bands. Nanda *et al.* (2020) showed that the

598    operational algorithm of TROPOMI operational algorithm can provide ALH pixel

599    retrievals only for scenes dominated by absorbing aerosol particles. In addition, Griffin

600    *et al.* (2020) reported that the pixels with low positive UVAI values (weak absorbing

601    cases) are identified with low QA values ($QA \leq 0.5$) in the offline product of ALH.

602    Although the TROPOMI ALH algorithm updated for the expansion of retrieval range,

603    the contrast of $O_2$-$O_2$ SCD to the aerosol layer height change is fundamentally weak

604    sensitivity in scattering dominant aerosols (e.g., Park et al., 2016). For this reason, the

605    bias and standard deviation of height difference between GEMS and ALH is generally

606    larger in high SSA.

607    In addition, the difference between GEMS AEH and TROPOMI ALH depends on

608    TYPE, as shown in Figure 15b. The difference was $1.47 \pm 1.15$, $1.46 \pm 0.98$, and $1.80 \pm$

609    1.32 km for "Absorbing", "Dust", and "Non-Absorbing" type aerosols, respectively.

610    Similar to Figure 13c, the TYPE dependence of aerosol height information was

611    influenced by both absorptivity and size information. "Dust" type of aerosol is mainly

612    transported in the free troposphere with gaussian-like vertical distribution, and the

613    associated plume thickness is highly variable. However, "Absorbing" aerosols mainly

614    originate from anthropogenic emissions in East Asia and mostly distributed near the

615    surface with homogeneous concentration (e.g., Gao *et al.*, 2014; Wang *et al.*, 2012;

616    Peng *et al.*, 2016). Transport patterns and vertical distribution shape depending on

617    aerosol types, can affect the accuracy of aerosol height retrieval results.

618
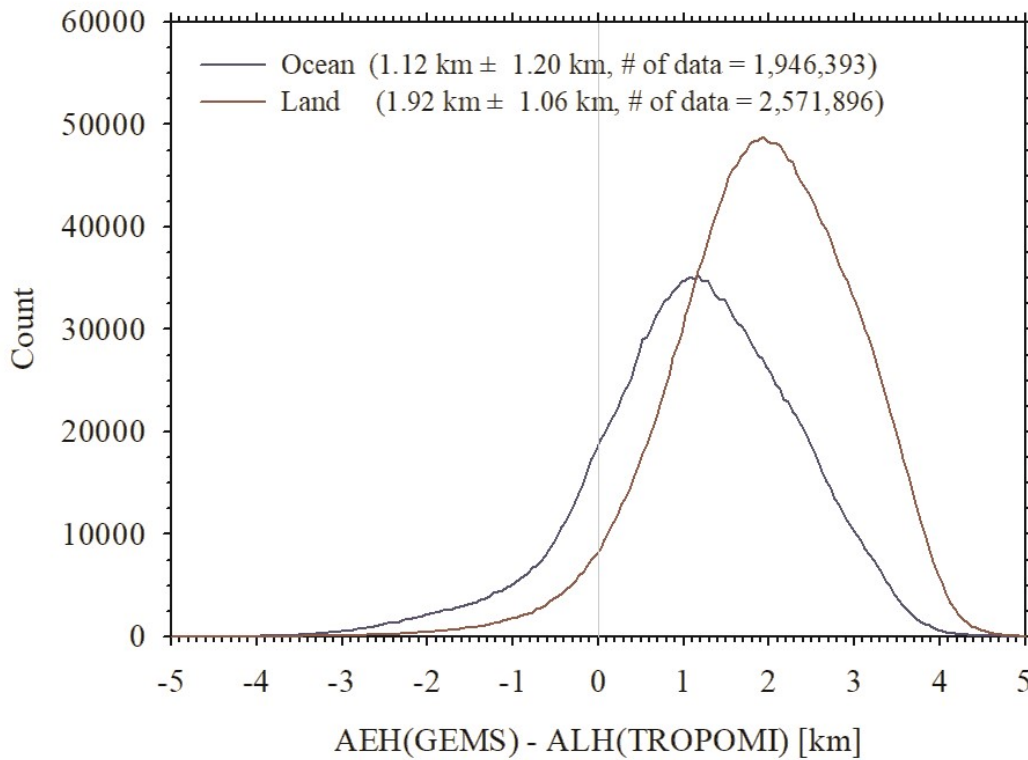
619    **Figure 16.** Histogram of the difference between TROPOMI ALH and GEMS AEH

620    over land and ocean pixels, respectively, from January 1 to June 30, 2021.

621

622    The non-Lambertian effect on the land surface impacted surface reflectance

623    uncertainty during AEH retrieval, and this effect led to bias and variance in AEH. In this

624    study, the minimum Lambertian equivalent reflectance was used as the reference

625    reflectance value. However, surface reflectivity has geometric dependence due to non-

626    Lambertian effects, which leads to a bias of 0.01-0.02 for surface reflectance over the

627    land surface (e.g., Qin *et al.*, 2019). To identify the sensitivity of surface property, a

628    histogram was constructed of difference between GEMS AEH and TROPOMI ALH

629 after classification into land and ocean surface types, as shown in Figure 16. From the

630 statistical results, the mean differences were estimated to be 1.12 ± 1.20 and 1.92 ± 1.06

631 km for ocean and land pixels, respectively. The bias has significant difference between

632 two different surface types. Michailidis et al. (2023) explained that the experimental

633 retrieval range of ALH from TROPOMI is 0.27-6.5 km and 0.06-2.15 km over ocean

634 and land, respectively. Constrained retrieval range over land by the TROPOMI

635 influences the negative bias of aerosol height retrieval and increases the mean difference

636 of aerosol height between GEMS and TROPOMI. In addition, the non-Lambertian

637 effect for surface reflectance is also affecting the increasing discrepancy of aerosol

638 height information.
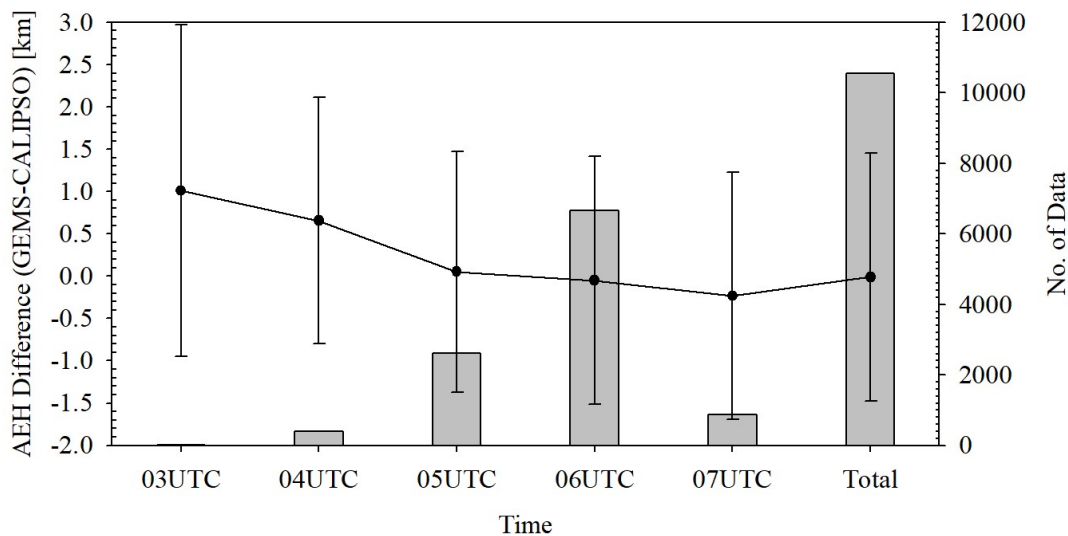
640 **Figure 17.** Diurnal dependence of AEH difference between CALIOP and GEMS

641 from January 1 to June 30, 2021 (Black dots and error bars denote the mean and

642 standard deviation of AEH difference, while the gray-box indicates the number of data).

643

644 The results of hourly statistical analyses are presented in Figure 17. Because they use

645    a consistent definition of AEH, we show only a comparison of GEMS and CALIOP. The

646    diurnal variation in AEH difference ranged from -0.23 ± 1.45 km (07:00 UTC, Number

647    of Data = 867) to 1.01 ± 1.96 km (03:00 UTC, Number of Data = 23). However, the

648    number of pixels observed at 03:00 UTC was insufficient for the identification of

649    diurnal variation of retrieval uncertainty. The AEH difference of 0.66 ± 1.45 km was the

650    next highest value obtained at 04:00 UTC (Number of Data = 395). The inhomogeneous

651    number of data is mainly due to the lack of spatial homogeneity among retrieval pixels.

652    Over India, very high AOD values were consistently observed during the comparison

653    period. Otherwise, the AEH was only retrieved under conditions of severe

654    anthropogenic emissions over East Asia. In addition, the diurnal variation in AEH

655    difference was caused by spatial characteristics of AEH difference. From 03:00 to 05:00

656    UTC, CALIOP mainly passed over East Asia, which has numerous sources of aerosol

657    emissions, including biomass burning, dust, and industrial activity. In addition, GEMS

658    observed only the eastern part of India, which is dominated by anthropogenic aerosols.

659    The spatial distribution of the dominant aerosol types may impact the diurnal variation

660    in AEH difference.

661

662    **6. Summary & Conclusions**

663    Based on the possibility of retrieving AEH from environmental satellite sensors, an

664    AEH retrieval algorithm for GEMS was developed that solely uses the $O_2$-$O_2$ absorption

665    band with considering of aerosol and surface properties. Because the sensitivity of AEH

666    retrieval is strongly affected by optical depth and properties of aerosols, as well as

667    surface reflectivity, the AEH retrieval algorithm for GEMS uses the GEMS operational

668    product, L2AERAOD. With the newly developed retrieval algorithm, GEMS can be

669  used to monitor aerosol vertical information with high temporal and spatial resolution.

670  For dust plumes over East Asia, AEH retrieval results from GEMS indicated

671  appropriated aerosol vertical information. After spatial and temporal colocation, the

672  AEH from GEMS aligned well with the AEH information obtained from CALIOP. The

673  differences in AEH between GEMS and CALIOP for dust plume cases were -0.13 $\pm$

674  1.32 and -0.15 $\pm$ 0.97 km, with 49.9-75.9% and 73.2-86.7% of all pixels showing

675  differences less than 1.0 and 1.5 km, respectively. Large AEH uncertainty was found

676  mostly over inland China due to uncertainty in surface reflectance and AOD over the

677  land surface. In addition, AEH from GEMS was overestimated compared to the

678  TROPOMI ALH results. The overestimation is partially caused by different definitions

679  of ALH from TROPOMI and AEH from GEMS.

680  In long-term intercomparison with CALIOP, the average AEH difference was

681  estimated to be -0.03 km, with a standard deviation of 1.4 km under the scenario of

682  AOD > 0.4. The large variation in AEH difference between GEMS and CALIOP was

683  caused by uncertainty in the input parameters estimated from L2AERAOD. In the long-

684  term intercomparison against TROPOMI, this difference was dependent on both SSA

685  and TYPE. The difference was 1.50 $\pm$ 1.08 km, 1.59 $\pm$ 1.22 km, and 1.71 $\pm$ 1.24 km for

686  pixels with SSA < 0.90, 0.90 < SSA < 0.95, and SSA > 0.95, respectively. In addition,

687  differences of 1.47 $\pm$ 1.15 km, 1.46 $\pm$ 0.98 km, and 1.80 $\pm$ 1.32 km were obtained for

688  the "Absorbing", "Dust", and the "Non-Absorbing" types of aerosols, respectively. The

689  AEH difference also has diurnal dependence, which ranged from -0.23 $\pm$ 1.45 km to

690  1.01 $\pm$ 1.96 km, due to the spatial characteristics of dominant aerosol types.

691  The case studies and results of the long-term validation show that AEH retrieved

692  from GEMS can provide information on aerosol vertical distribution, with applications

693    in diverse research fields. The AEH results with long-term statistical accuracy make it

694    possible to use the application study for AMF calculation of GEMS trace gas retrieval.

695    In addition, AEH considerably affects the surface particulate matter (PM) concentration

696    obtained from satellite-based AOD because PM estimation is significantly affected by

697    the mixing layer height of aerosols. For this reason, the AEH can provide effective

698    mixing layer height of aerosols for anthropogenic aerosols and also provide the vertical

699    patterns for long-range transport of aerosols.

700    Although several fields of study may apply the AEH retrieval results, retrieval

701    uncertainty in AEH remains due to the uncertainty of retrieved AOD and SSA. In

702    addition, the uncertainty in surface reflectance and the discrepancy in $O_2$-$O_2$ SCD

703    values between the simulation results and observations can be affected to the potential

704    error sources of AEH from GEMS. To minimize the AEH retrieval uncertainty, further

705    analysis related to the optimized input parameters of AOD, SSA, and aerosol type

706    information is essential. For this reason, the quantitative analysis of AEH uncertainty

707    due to aerosol and surface property is important for the improvement of AEH retrieval

708    algorithm. In addition, aerosol optical property retrieval by the visible channel will be

709    needed for further study to improve the aerosol type determination. Although the

710    aerosol indices of UV and visible provide the aerosol type information, developing the

711    aerosol type classification algorithm is necessary to make synergy with AEH retrieval.

712    AEH provides representative layer height information as only one variable because of

713    its sole reliance on $O_2$-$O_2$ SCD for direct estimation of aerosol height information. This

714    method is limited to the consideration of aerosol vertical structures (i.e., Gaussian or

715    exponential vertical distribution structures). To increase the information contents, it

716    would be valuable to combine other oxygen absorption bands from other satellite

717    instruments together with extinction information of aerosols.

718

719    **Data Availability**

720    The TROPOMI ALH product is available from http://doi.org/10.5270/S5P-7g4iapn,

721    and the CALIOP aerosol extinction profile product is available from

722    https://doi.org/10.5067/CALIOP/CALIPSO/CAL_LID_L2_05kmAPro-Prov-V3-41.

723    The GEMS AEH and AERAOD products are available from the Environmental Satellite

724    Center in National Institute of Environmental Research (NIER) of the Republic of

725    Korea.

726

727    **Acknowledgements**

728    This work was supported by the National Institute of Environment Research of the

729    Republic of Korea under Grant NIER-2023-04-02-050.

730

## References

731 **References**

732 Accarreta, J. R., de Haan, J. F., and Stammes, P.: Cloud pressure retrieval using the O2-
733     O2 absorption band at 477 nm, J. Geophys. Res., 109, D05204,
734     doi:10.1029/2003JD003915, 2004

735 Ahn, C., Torres, O., and Jethva, H.: Assessment of OMI near-UV aerosol optical depth
736     over land, J. Geophys. Res., 119, 2457-2473, 2014.

737 Bogumil, K., Orphal, J., Burrows, J. P., and Flaud, J. M.: Vibrational progressions in the
738     visible and near-ultraviolet absorption spectrum of ozone, Chem. Phys. Lett., 349,
739     241-248, 2001.

740 Buchard, V., de Silva, A. M., Colarco, P. R., Darmenov, A., Randles, C. A., Govindaraju,
741     R., Torres, O., Campbell, J., and Spurr, R.: Using the OMI aerosol index and
742     absorption aerosol optical depth to evaluate the NASA MERRA Aerosol reanalysis,
743     Atmos. Chem. Phys., 15, 5743-5760, 2015.

744 Chen, X., Wang, J., Xu, X., Zhou, M., Zhang, H., Garcia, L. C., Colarco, P. R., Janz, S.
745     J., Yorks, J., McGill, M., Reid, J. S., de Graaf, M., and Kondragunta, S.: First
746     retrieval of absorbing aerosol height over dark target using TROPOMI oxygen B
747     band: Algorithm development and application for surface particulate matter
748     estimates, Remote Sens. Env., 265, 112674, 2021.

749 Chen, X., Xu, X., Wang, J., and Diner, D. J.: Can Multi-angular polarimetric
750     measurements in the oxygen-A and B bands improve the retrieval of aerosol
751     vertical distribution?, J. Quant., Spectro. Rad. Trans., 270, 107679, 2021.

752 Chimot, J., Veefkind, J. P., Vlemmix, T., de Haan, J. F., Amiridis, V., Proestakis, E.,
753     Marinou, E., and Levelt, P. F.: An exploratory study on the aerosol height retrieval
754     from OMI measurements of the 477 nm O2-O2 spectral band using a neural
755     network approach, Atmos. Meas. Tech., 10, 783-809, 2017.

756 Choi, H., Liu, X., Abad, G. G., Seo, J., Lee, K. -M., and Kim, J.: A fast retrieval of
757     cloud parameters using a Triplet of wavelengths of oxygen dimer band around 477
758     nm, Remote Sens., 13, 152, doi: 10.3390/rs13010152, 2021.

759 Choi, W., Lee, H., Kim, J., Ryu, J. -Y., Park, S. S., Park, J., and Kang, H.: Effects of
760     spatiotemporal O4 column densities and temperature-dependent O4 absorption
761     cross-section on an aerosol effective height retrieval algorithm using the O4 air

762    mass factor from the ozone monitoring instrument, Remote Sens. Env., 229, 223-
763        233, 2019.

764    Choi, W., Lee, H., and Kim, J.: First TROPOMI retrieval of aerosol effective height
765        using O4 absorption band at 477 nm and aerosol classification, IEEE Trans.
766        Geosci., Remote Sens., 59, 9873-9886, 2021.

767    de Graaf, M., Stammes, P., Torres, O., and Koelemeijer, R. B. A.: Absorbing aerosol
768        index: Sensitivity analysis, application to GOME and comparison with TOMS, J.
769        Geophys. Res., 110, D01201, doi:10.1029/2004JD005178, 2005.

770    de Graaf, M., de Haan, J. F., and Sanders, A. F. J.: TROPOMI ATBD of the Aerosol
771        Layer        Height,        issue        2.4.0,        2022-04-08,
772        https://sentinel.esa.int/documents/247904/2476257/Sentinel-5P-TROPOMI-
773        ATBD-Aerosol-Height, 75pp, Royal Netherlands Meteorological Institute,
774        Netherland, last access: 15 June, 2024.

775    Ding, S., Wang, J., and Xu, X.: Polarimetric remote sensing in oxygen A and B bands:
776        Sensitivity study and information content analysis for vertical profile of aerosols,
777        Atmos. Meas. Tech, 9, 2077-2092, 2016.

778    Dubuisson, P., Frouin, R., Dessaily, D., Duforet, L., Leon, J. –F., Voss, K., and Antoine,
779        D.: Estimating the altitude of aerosol plumes over the ocean from reflectance ratio
780        measurements in the O2 A-band, Remote Sens. Environ., 113, 1899-1911,
781        doi:10.1016/j.rse.2009.04.018, 2009.

782    European Space Agency, *TROPOMI Level 2 Aerosol Layer Height products. Version*
783        *02.* https://doi.org/10.5270/S5P-7g4iapn, 2021.

784    Gao, Y., Zhao, C., Liu, X., Zhang, M., and Leung, L. R.: WRF-Chem simulations of
785        aerosols and anthropogenic aerosol radiative forcing in East Asia, Atmos. Environ.,
786        92, 250-266, 2014.

787    Geddes, A., and Boesch, H.: Tropospheric aerosol profile information from high-
788        resolution oxygen A-band measurements from space, Atmos. Meas. Tech., 8, 859-
789        874, 2015.

790    Go, S., Kim, J., Park, S. S., Kim, M., Lim, H., Kim, J. -Y., Lee, D. -W., and Im, J.:
791        Synergistic use of hyperspectral UV-visible OMI and broadband meteorological
792        imager MODIS data for a merged aerosol product, Remote Sens., 12, 3987,
793        doi:10.3390/rs12233987, 2020.

794  Griffin, D., Sioris, C., Chen, J., Dickson, N., Kovachik, A., de Graaf, M., Nanda, S.,
795      Veefkind, P., Dammers, E., McLinden, C. A., Makar, P., and Akingunola, A.: The
796      2018 fire season in North America as seen by TROPOMI: aerosol layer height
797      intercomparisons and evaluation of model-derived plume heights, Atmos. Meas.
798      Tech., 13, 1427-1445, 2020.

799  Herman, J. R., Bhartia, P. K., Torres, O., Hsu, C., Seftor, C., and Celarier, E.: Global
800      distribution of UV-absorbing aerosols from Nimbus-7/TOMS data, J. Geophys.
801      Res., 102(D14), 16911-16922, 1997.

802  Hong, H., Lee, H., Kim, J., Jeong, U., Ryu, J., and Lee, D. S.: Investigation of
803      simultaneous effects of aerosol properties and aerosol peak height on the air mass
804      factors for space-borne NO2 retrievals, Remote Sens., 9, 208,
805      doi:10.3390/rs9030208, 2017.

806  Joiner, J., and Bhartia, P. K.: The determination of cloud pressures from rotational
807      Raman scattering in satellite backscatter ultraviolet measurements, J. Geophys.
808      Res., 100, 23019-23026, 1995.

809  Joiner, J., and Vasilkov, A. P.: First results from the OMI rotational Raman scattering
810      cloud pressure algorithm, IEEE Trans. Geosci. Remote Sens., 44, 1272-1282, 2006.

811  Kim, M., Kim, J., Torres, O., Ahn, C., Kim, W., Jeong, U., Go, S., Liu, X., Moon, K. J.,
812      and Kim D. -R.: Optimal estimation-based algorithm to retrieve aerosol optical
813      properties for GEMS measurements over Asia, 10, 162, doi:10.3390/rs10020162,
814      2018.

815  Kim, J., Jeong, U., Ahn, M. -H., Kim, J. H., Park, R. J., Lee, H., Song, C. H., Choi, Y. -
816      S., Lee, K. -H., Yoo, J. -M., Jeong, M. -J., Park, S. K., Lee, K. -M., Song, C. -K.,
817      Kim, S. -W., Kim, Y. J., Kim, S. -W., Kim, M., Go, S., Liu, X., Chance, K., Chan
818      Miller, C., Al-Saadi, J., Veihelmann, B., Bhartia, P. K., Torres, O., González Abad,
819      G., Haffner, D. P., Ko, D. H., Lee, S. H., Woo, J. -H., Chong, H., Park, S. S., Nicks,
820      D., Choi, W. J., Moon, K. -J., Cho, A., Yoon, J., Kim, S. -K., Hong, H., Lee, K.,
821      Lee, H., Lee, S., Choi, M., Veefkind, P., Levelt, P. F., Edwards, D. P., Kang, M., Eo,
822      M., Bak, J., Baek, K., Kwon, H. -A., Yang, J., Park, J., Han, K. M., Kim, B. -R.,
823      Shin, H. -W., Choi, H., Lee, E., Chong, J., Cha, Y., Koo, J. -H., Irie, H., Hayashida,
824      S., Kasai, Y., Kanaya, Y., Liu, C., Lin, J., Crawford, J. H., Carmichael, G. R.,
825      Newchurch, M. J., Lefer, B. L., Herman, J. R., Swap, R. J., Lau, A. K. H., Kurosu,

T. P., Jaross, G., Ahlers, B., Dobber, M., McElroy, C. T., and Choi, Y.: New era of air quality from Space: Geostationary Environment Monitoring Spectrometer (GEMS), Bul. Ame. Meteorol. Soc., 101(1), E1–E22, 2020.

Koffi, B., Schulz, M., Bréon, F.-M., Griesfeller, J., Winker, D., Balkanski, Y., Bauer, S., Berntsen, T., Chin, M., Collins, W. D., Dentener, F., Diehl, T., Easter, R., Ghan, S., Ginoux, P., Gong, S., Horowitz, L. W., Iversen, T., Kirkevåg, A., Koch, D., Krol, M., Myhre, G., Stier, P., and Takemura, T.: Application of the CALIOP layer product to evaluate the vertical distribution of aerosols estimated by global models: AeroCom phase I results, J. Geophys. Res.-Atmos., 117, D10201, https://doi.org/10.1029/2011jd016858, 2012.

Kokhanovsky, A. A., and Rozanov, V. V.: The determination of dust cloud altitudes from a satellite using hyperspectral measurements in the gaseous absorption band, Int. J. Rem. Sens., 31, Nos. 9-10, 2729-2744, 2010.

Kooreman, M. L., Stammes, P., Trees, V., Sneep, M., Tilstra, L. G., de Graaf, M., Zweers, D. C. S., Wang, P., Tuinder, O. N. E., and Veefkind, J. P.: Effects of cloud on the UV absorbing aerosol index from TROPOMI, Atmos. Meas. Tech., 13, 6407-6426, 2020.

Lee, J., Kim, J., Song, C. H., Kim, S. B., Chun, Y., Sohn, B. J., and Holben, B. N.: Characteristics of aerosol types from AERONET sunphotometer measurements. Atmos. Env., 44, 3110-3117, 2010.

Lorente, A., Boersma, K. F., Yu, H., Doerner, S., Hilboll, A., Richter, A., Liu, M., Lamsal, L. N., Barkley, M., De Smedt, I., Van Roozendael, M., Wang, Y., Wagner, T., Beirle, S., Liu, J. -T., Krotkov, N., Stammes, P., Wang, P., Eskes, H. J., and Krol, M.: Structural uncertainty in air mass factor calculation for NO2 and HCHO satellite retrieval, Atmos. Meas. Tech., 10, 759-782, 2017.

Michailidis, K., Koukouli, M. -E., Balis, D., Veefkind, J. P., de Graaf, M., Mona, L., Papagianopoulos, N., Pappalardo, G., Tsikoudi, I., Amiridis, V., Marinou, E., Gialitaki, A., Mamouri, R. -E., Nisantzi, A., Bortoli, D., Joao Costa, M., Salgueiro, V., Papayannis, A., Mylonaki, M., Alados-Arboledas, L., Romano, S., Perrone, M. R., and Baars, H.: Validation of the TROPOMI/S5P aerosol layer height using EARLINET lidars, Atmos. Chem. Phys., 23, 1919-1940, 2023.

857     Nanda, S., de Graaf, M., Sneep, M., de Haan, J. F., Stammes, P., Sanders, A. F. J.,
858          Tuinder, O., Veefkind, J. P., and Levelt, P. F.: Error sources in the retrieval of
859          aerosol information over bright surfaces from satellite measurements in the oxygen
860          A band, Atmos. Meas. Tech., 11, 161–175, https://doi.org/10.5194/amt-11-161-
861          2018, 2018.

862     Nanda, S., de Graaf, M., Veefkind, J. P., Sneep, M., ter Linden, M., Sun, J., and Level, P.
863          F.: A first comparison of TROPOMI aerosol layer height (ALH) to CALIOP data,
864          Atmos. Meas. Tech., 13, 3043-3059, 2020.

865     National Institute of Environmental Research, Geostationary Environment Monitoring
866          Spectrometer (GEMS) Algorithm Theoretical Basis Document: Aerosol Retrieval
867          Algorithm, 42pp, Ministry of Environment, Korea, 2020.

868     Omar, A., Winker, D. M., Vaughan, M. A., Ju, Y., Trepte, C. R., Ferrare, R. A., Lee, K.-
869          P., Hostetler, C. A., Kittaka, C., Rogers, R. R., Kuehn, R. E., and Liu, Z.: The
870          CALIPSO automated aerosol classification and Lidar ratio selection algorithm, J.
871          Atmos. Ocean. Tech., 26, 10, 1994-2014, 2009.

872     Park, S. S., Kim, J., Lee, H., Torres, O., Lee, K. –M., and Lee, S. D.: Utilization of O4
873          slant column density to derive aerosol layer height from a space-borne UV-visible
874          hyperspectral sensor: Sensitivity and case study, Atmos. Chem. Phys., 16, 1987-
875          2006, doi:10.5194/acp-16-1987-2016, 2016.

876     Park, S. S., Takemura, T., and Kim, J.: Effect of temperature-dependent cross sections
877          on O4 slant column density estimation by a space-borne UV-visible hyperspectral
878          sensor, Atmos. Environ., 152, 98-110, 2017.

879     Park, S. S., Kim, S. -W., Song, C. -K., Park, J. -U., and Bae, K. -H.: Spatio-temporal
880          variability of aerosol optical depth, total ozone, and NO2 over East Asia: Strategy
881          for the validation to the GEMS Scientific Products, Remote Sens., 12, 2256, 2020.

882     Peng, J., Hu, M., Guo, S., Du, Z., Zheng, J., Shang, D., Zamora, M. L., Zeng, L., Shao,
883          M., Wu, Y. -S., Zheng, J., Wang, Y., Glen, C. R., Collins, D. R., Molina, M. J., and
884          Zhang R.: Markedly enhanced absorption and direct radiative forcing of black
885          carbon under polluted urban environments, Proc. Natl. Acad. Sci., 113, 4266-4271,
886          2016.

887 Penning de Vries, M. J. M., Beirle, S., and Wagner, T.: UV aerosol indices from
888     SCIAMACHY: Introducing the Scattering Index (SCI), Atmos. Chem. Phys., 9,
889     9555-9567, 2009.

890 Penning de Vries, M. J. M., Beirle, S., Hoermann, C., Kaiser, J. W., Stammes, P., Tilstra,
891     L. G., Tuinder, O. N. E., and Wagner, T.: A global aerosol classification algorithm
892     incorporating multiple satellite data sets of aerosol and trace gas abundances,
893     Atmos. Chem. Phys., 15, 10597-10618, 2015.

894 Prospero, J. M., Ginoux, P., Torres, O., Nicholson, S. E., and Gill T. E.: Environmental
895     characterization of global sources of atmospheric soil dust identified with the
896     Nimbus 7 total ozone mapping spectrometer (TOMS) absorbing aerosol product,
897     Rev. Geophys., 40, 1002, doi:10.1029/2000RG000095, 2002.

898 Qin, W., Fasnacht, Z., Haffner, D., Vasilkov, A., Joiner, J., Krotkov, N., Fisher, B., and
899     Spurr, R.: A geometry-dependent surface Lambertian-equivalent reflectivity
900     product for UV-vis retrievals – Part 1: Evaluation over land surfaces using
901     measurements from OMI at 466 nm, Atmos. Meas. Tech., 12, 3997-4017, 2019.

902 Rana, A., Jia, S., and Sarkar, S.: Black carbon aerosol in India: A comprehensive review
903     of current status and future prospects, Atmos. Res., 218, 207-230, 2019.

904 Sanders, A. F. J., de Haan, J. F., Sneep, M., Apituley, A., Stammes, P., Vieitez, M. O.,
905     Tilstra, L. G., Tuinder, O. N. E., Koning, C. E., and Veefkind, J. P.: Evaluation of
906     the operational Aerosol Layer Height retrieval algorithm for Sentinel-5 Precursor:
907     application to O2 A band observations from GOME-2A, Atmos. Meas. Tech., 8,
908     4947-4977, 2015.

909 Sanders, A. F. J. and de Haan, J. F.: TROPOMI ATBD of the Aerosol Layer Height
910     product, 2016.

911 Sanghavi, S., Martonchik, J. V., Landgraf, J., and Platt, U.: Retrieval of optical depth
912     and vertical distribution of particulate scatterers in the atmosphere using O2 A- and
913     B-band SCIAMACHY observations over Kanpur: A case study, Atmos. Meas.
914     Tech., 5, 1099-1119, 2012.

915 Spurr, R. "User's Guide VLIDORT Version 2.6, RT Solutions.", Cambridge, MA,
916     USA, 2013.

917     Spurr, R., and Christri, M.: On the generation of atmospheric property Jacobians from
918          the (V)LIDORT linearized radiative transfer models, J. Quant. Spectrosc. Radiat.
919          Transf., 142, 109-115, 2014.

920     Thalman, R., and Volkamer, R.: Temperature dependent absorption cross-sections of
921          O2-O2 collision pairs between 340 and 630 nm and at atmospherically relevant
922          pressure. Phys. Chem. Chem. Phys. 15, 15371e15381, 2013.

923     Torres, O., Bhartia, P. K., Herman, J. R., Ahmad, Z., and Gleason, J.: Derivation of
924          aerosol properties from satellite measurements of backscattered ultraviolet
925          radiation: Theoretical basis, J. Geophys. Res., 103(14), 17099-17110, 1998.

926     Torres, O., Decae, R., Veefkind, P., and de Leeuw, G.: OMI Aerosol Retrieval Algorithm,
927          OMI Algorithm Theoretical Basis Document, Vol. III, Clouds, Aerosols and
928          Surface UV Irradiance, NASA-KNMI ATBD-OMI-03, pp. 47-71, 2002.

929     Torres, O., Jethva, H., Ahn, C., Jaross, G., and Loyola, D. G.: TROPOMI aerosol
930          products: evaluation and observations of synoptic-scale carbonaceous aerosol
931          plumes during 2018-2020, Atmos. Meas. Tech., 13, 6789-6806, 2020.

932     Vandaele, A. C., Hermans, C., Simon, P. C., Carleer, M., Colin, R., Fally, S., Merienne,
933          M. F., Jenouvrier, A., and Coquart, B.: Measurements of the NO2 absorption cross-
934          section from 42000 cm-1 to 10000 cm-1 (238-1000 nm) at 220 K and 294 K, J.
935          Quant. Spectrosc. Radiat. Transfer, 59, 3-5, 171-184, 1998.

936     Vasilkov, A., Joiner, J., Spurr, R., Bhartia, P. K., Levelt, P., and Stephens, G.: Evaluation
937          of the OMI cloud pressures derived from rotational Raman scattering by
938          comparisons with other satellite data and radiative transfer simulations, J. Geophys.
939          Res., 113, D15S19, doi:10.1029/2007JD008689, 2008.

940     Vasilkov, A., Yang, E. -S., Marchenko, S., Qin, W., Lamsal, L., Joiner, J., Krotkov, N.,
941          Haffner, D., Bhartia, P. K., and Spurr, R.: A cloud algorithm based on the O2-O2
942          477 nm absorption band featuring an advanced spectral fitting method and the use
943          of surface geometry-dependent Lambertian-equivalent reflectivity, Atmos. Meas.
944          Tech., 11, 4093-4107, 2018.

945     Veefkind, J. P., Aben, I., McMullan, K., Foerster, H., de Vries, J., Otter, G., Claas, J.,
946          Eskes, H. J., de Haan, J. F., Kleipool, Q., van Weele, M., Hasekamp, O.,
947          Hoogeveen, R., Landgraf, J., Snel, R., Tol, P., Ingmann, P., Voors, R., Kruizinga, B.,
948          Vink, R., Visser, H., and Levelt, P. F.: TROPOMI on the ESA Sentinel-5 Precursor:

A GMES mission for global observations of the atmospheric composition for climate, air quality and ozone layer applications, Remote Sens. Env., 120, 70-83, 2012.

Veihelmann, B., Levelt, P. F., Stammes, P., and Veefkind, J. P.: Simulation study of the aerosol information content in OMI spectral reflectance measurements, Atmos. Chem. Phys., 7, 3115-3127, 2007.

Wang, R., Tao, S., Wang, W., Liu, J., Shen, H., Shen, G., Wang, B., Liu, X., Li, W., Huang, Y., Zhang, Y., Lu, Y., Chen, H., Chen, Y., Wang, C., Zhu, D., Wang, X., Li, B., Liu, W., and M, J.: Black carbon emissions in China from 1949 to 2050, Environ., Sci. Technol., 46, 7595-7603, 2012.

Winker, D. M., Vaughan, M. A., Omar, A. H., Hu, Y., Powell, K. A., Liu, Z., Hunt, W. H., and Young, S. A.: Overview of the CALIPSO mission and CALIOP data processing algorithms, J. Atmos. Oceanic Technol., 26, 2310-2323, 2009.

Xu, X., Wang, J., Yang, Y., Zeng, J., Torres, O., Yang, Y., Marshak, A., Reid, J., and Miller, S.: Passive remote sensing of altitude and optical depth of dust plumes using the oxygen A and B bands: First results from EPIC/DSCOVR at Lagrange-1 point, Geophys. Res. Lett., 44, 7544-7554, 2017.

Xu, X., Wang, J., Wang, Y., Zeng, J., Torres, O., Reid, J. S., Miller, S. D., Martins, J. V., and Remer, L. A.: Detecting layer height of smoke aerosols over vegetated land and water surfaces via oxygen absorption bands: hourly results from EPIC/DSCOVR in deep space, Atmos. Meas. Tech., 12, 3269-3288, 2019.

Zeng, Z. -C., Chen, S., Natraj, V., Le, T., Xu, F., Merrelli, A., Crisp, D., Sander, S. P., and Yung, Y. L.: Constraining the vertical distribution of coastal dust aerosol using OCO-2 O2 A-band measurements, Remote Sens. Env., 236, 111494, 2020.